

A Bluetooth Low-Energy Transceiver with 3.7-mW All-Digital Transmitter, 2.75-mW High-IF Discrete-Time Receiver, and TX/RX Switchable On-Chip Matching Network

Kuo, Feng-Wei; Binsfeld Ferreira, Sandro; Chen, Huan-Neng Ron; Cho, Lan-Chou; Jou, Chewn-Pu; Hsueh, Fu-Lung; Madadi, Iman; Tohidian, Massoud; Shahmohammadi, Mina; Babaie, Masoud

DOI

[10.1109/JSSC.2017.2654322](https://doi.org/10.1109/JSSC.2017.2654322)

Publication date

2017

Published in

IEEE Journal of Solid State Circuits

Citation (APA)

Kuo, F.-W., Binsfeld Ferreira, S., Chen, H.-N. R., Cho, L.-C., Jou, C.-P., Hsueh, F.-L., Madadi, I., Tohidian, M., Shahmohammadi, M., Babaie, M., & Staszewski, R. B. (2017). A Bluetooth Low-Energy Transceiver with 3.7-mW All-Digital Transmitter, 2.75-mW High-IF Discrete-Time Receiver, and TX/RX Switchable On-Chip Matching Network. *IEEE Journal of Solid State Circuits*, 52(4), 1144-1162. Article 7862859. <https://doi.org/10.1109/JSSC.2017.2654322>

Important note

To cite this publication, please use the final published version (if applicable). Please check the document version above.

Copyright

Other than for strictly personal use, it is not permitted to download, forward or distribute the text or part of it, without the consent of the author(s) and/or copyright holder(s), unless the work is under an open content license such as Creative Commons.

Takedown policy

Please contact us and provide details if you believe this document breaches copyrights. We will remove access to the work immediately and investigate your claim.

A Bluetooth Low-Energy Transceiver With 3.7-mW All-Digital Transmitter, 2.75-mW High-IF Discrete-Time Receiver, and TX/RX Switchable On-Chip Matching Network

Feng-Wei Kuo, Sandro Binsfeld Ferreira, *Member, IEEE*, Huan-Neng Ron Chen, Lan-Chou Cho, Chewn-Pu Jou, *Member, IEEE*, Fu-Lung Hsueh, *Life Member, IEEE*, Iman Madadi, *Member, IEEE*, Massoud Tohidian, *Member, IEEE*, Mina Shahmohammadi, *Member, IEEE*, Masoud Babaie, *Member, IEEE*, and Robert Bogdan Staszewski, *Fellow, IEEE*

Abstract—We present an ultra-low-power Bluetooth low-energy (BLE) transceiver (TRX) for the Internet of Things (IoT) optimized for digital 28-nm CMOS. A transmitter (TX) employs an all-digital phase-locked loop (ADPLL) with a switched current-source digitally controlled oscillator (DCO) featuring low frequency pushing, and class-E/F₂ digital power amplifier (PA), featuring high efficiency. Low 1/f DCO noise allows the ADPLL to shut down after acquiring lock. The receiver operates in discrete time at high sampling rate (~10 Gsamples/s) with intermediate frequency placed beyond 1/f noise corner of MOS devices. New multistage multirate charge-sharing bandpass filters are adapted to achieve high out-of-band linearity, low noise, and low power consumption. An integrated on-chip matching network serves to both PA and low-noise transconductance amplifier, thus allowing a 1-pin direct antenna connection with no external band-selection filters. The TRX consumes 2.75 mW on the RX side and 3.7 mW on the TX side when delivering 0 dBm in BLE.

Index Terms—All-digital PLL (ADPLL), Bluetooth low energy (BLE), digitally controlled oscillator (DCO), discrete-time (DT) receiver (RX), Gaussian frequency shift keying (GFSK), intermediate frequency (IF), Internet of Things (IoT), low-power (LP) transceiver (TRX), matching network, transmit/receive (T/R) switch, transmitter (TX).

Manuscript received August 9, 2016; revised November 8, 2016 and December 22, 2016; accepted January 9, 2017. Date of publication February 23, 2017; date of current version March 23, 2017. This paper was approved by Guest Editor Brian Ginsburg. This work was supported in part by CAPES Foundation, Ministry of Education of Brazil (Process: 99999.011662/2013-01), in part by the European Research Council Consolidator under Grant 307624 TDRFSP, and in part by the Science Foundation Ireland under Grant 14/RP/I2921.

F.-W. Kuo, H.-N. R. Chen, L.-C. Cho, C.-P. Jou, and F.-L. Hsueh are with Taiwan Semiconductor Manufacturing Company, Hsinchu 300-77, Taiwan.

S. Binsfeld Ferreira was with the Federal University of Rio Grande do Sul, Porto Alegre 91501-970, Brazil, and also with the Delft University of Technology, 2628 Delft, The Netherlands.

I. Madadi, M. Tohidian, M. Shahmohammadi, and M. Babaie are with the Delft University of Technology, 2628 Delft, The Netherlands.

R. B. Staszewski was with the Delft University of Technology, 2628 Delft, The Netherlands, and is now with University College Dublin, Dublin 4, Ireland.

Color versions of one or more of the figures in this paper are available online at <http://ieeexplore.ieee.org>.

Digital Object Identifier 10.1109/JSSC.2017.2654322

I. INTRODUCTION

ULTRA-LOW-POWER (ULP) wireless transceivers (TRXs) for the Internet of Things (IoT) are a subject of intensive research in both industry and academia [1]–[10]. Bluetooth low energy (BLE) [11] is currently the most popular standard for short-range IoT communications. BLE is an extension of the conventional Bluetooth (BT) that specifies an increased channel spacing of 2 MHz and a relaxed interference tolerance to allow for low-power (LP) implementations. This paper focuses on implementing such a TRX in the most advanced low-cost bulk CMOS technology node: LP polysilicon gate version of 28-nm CMOS with nine metal layers. The key objective is to maximally reduce the system cost by fully integrating all the RF TRX building blocks, including the traditionally troublesome antenna-interfacing circuitry, such as the power amplifier (PA) matching network and transmit/receive (T/R) switch, while maximally reducing the power consumption.

To address the above objectives of full system integration at ULP consumption, including amenability with digital processors [6] in face of strong push toward a sub-threshold operation [12], the proposed TRX exploits all-digital and digitally intensive architectures for the frequency synthesizer, transmitter (TX), and receiver (RX) [13], [14]. A time-to-digital converter (TDC) in an all-digital PLL (ADPLL) employs a string of inverters to convert a time difference between reference and variable (RF) clocks into a digital phase error. Power consumption and resolution of the TDC improve with technology scaling. Furthermore, at the same area, device matching improves thus reducing TDC nonlinearity and the level of fractional spurs. On the RX side, most of signal processing and filtering is done using discrete-time (DT) passive switched capacitor circuits. Waveforms required for driving the switches are also generated using digital logic. To provide signal gain, DT techniques use inverter-based g_m cells that are always compatible with digital technology.

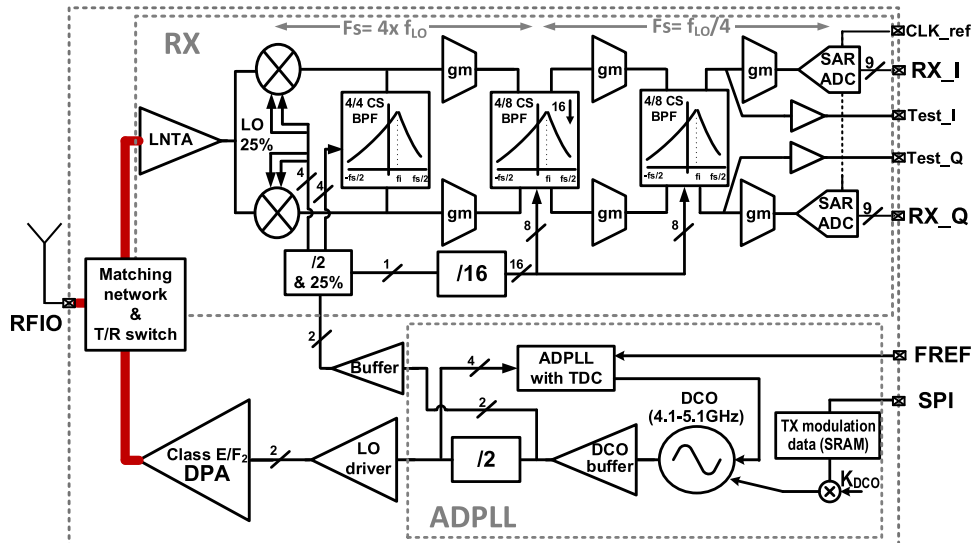


Fig. 1. Block diagram of the proposed BLE TRX.

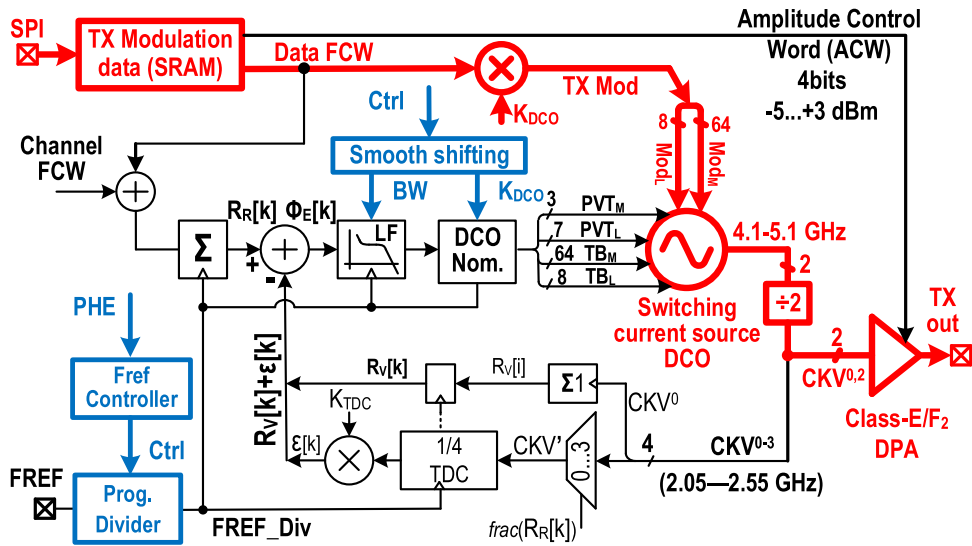


Fig. 2. Block diagram of the ADPLL-based TX. Red bold blocks: open-loop DCO modulation. Blue bold blocks: dynamic downscaling of the reference frequency.

As the technology scales, MOS switches become faster with lower parasitic capacitance [15], [16]. Consequently, digital waveform generators also become faster and more power efficient. On the other hand, metal capacitor density improves by migrating to more advanced technology, resulting in a reduced area. The above reasoning justifies the use of relatively advanced technology node of the 28-nm bulk CMOS in this paper, especially given an upcoming introduction of embedded nonvolatile memory.

Consequently, we have revisited the basic operation of major TRX building blocks—local oscillator (LO), TX, and RX—from the standpoint of power consumption for the relatively relaxed BLE performance (and IoT in general), and attempted to rearchitect the RF circuitry, given the objectives of advanced CMOS technology and full monolithic integration [9]. The LO and TX parts are largely based on a standalone TX published recently in [17] and [18],

so only a quick LO/TX summary and new features are covered here.

II. BRIEF OVERVIEW OF TRANSCIEVER ARCHITECTURE

Fig. 1 shows a block diagram of the BLE TRX. It successfully integrates all the required RF and IF building blocks and further adds a T/R antenna switch with an adjustable digital PA (DPA) and a low-noise transconductance amplifier (LNTA) matching networks such that the RF input/output (RFIO) pin can be directly connected to the antenna.

The LO shown in Fig. 2 is an ADPLL based on a switched current-source digitally controlled oscillator (DCO) [19] and a phase-predictive TDC [18]. The sensitivity of the RF oscillator to the common-mode noise (e.g., flicker noise of the oscillator transistors and supply modulation) is the main origin of the oscillator's flicker noise upconversion and frequency pushing. It is relatively well known that oscillators

with lower $1/f^3$ phase noise (PN) corner are also less sensitive to the supply/load modulation and thus frequency pushing and pulling [20]. While the reasons for a low flicker noise upconversion of the switching current source oscillator have been already discussed in depth in [18] and [21], this paper deals with its low frequency supply pushing. Contrary to the traditional cross-coupled oscillators, supply perturbations here cannot directly modulate gate–source voltage V_{gs} of M_{1-4} devices (see [18, Fig. 7]). Note that V_B biasing does not consume any dc current; therefore, realizing an on-chip V_B voltage reference with a good PSRR would be quite straightforward. Consequently, supply perturbations cannot modulate the oscillator’s dc current and nonlinear gate–source capacitance (C_{gs}) of M_{1-4} devices. Furthermore, the upper pair transistors just work in the cutoff, subthreshold, and saturation regions. The variation of gate–drain capacitance is almost negligible in these regions. As a result, the frequency pushing here is at least an order of magnitude better compared with the traditional structures.

The lower frequency pushing allows the ADPLL loop to be frozen after acquiring lock since the packet duration of $\sim 500 \mu s$ (and up to several milliseconds) will not incur any significant frequency drift.

The TX uses a dedicated DCO switchable capacitor bank ($Mod_{M/L}$ in Fig. 2) to perform direct GFSK modulation, while providing an option of also feeding the GFSK data to the second compensating feed (Data FCW) if the ADPLL is not frozen (i.e., two-point modulation). The DPA is realized as a switched-mode class-E/ F_2 topology with a transformer-based matching network, which was found to maximally enhance its efficiency at low supply voltage [22]. The TX architecture is also described in detail in [18].

This paper introduces a number of architecture- and circuit-level innovations to maximally reduce power and cost (i.e., maximum integration and lowest die area) of the BLE TRX. The transformers for the DCO and DPA are redesigned to incorporate the associated active devices underneath them with no significant loss of performance or power efficiency. This leads to a $>30\%$ reduction in the TX area.

The key innovation in the RX architecture was derived from realizing that the best devices and basic building blocks in low-voltage deep-nanoscale CMOS are logic gates, transistor switches, inverter-like g_m transconductors, and metal–oxide–metal (MOM) capacitors [15]. Hence, the most logical topology would be a charge-domain switched capacitor network operating in DT. However, to maximally reduce power consumption, MOS devices would need to be remarkably small, which would invariably increase their flicker noise corner. To mitigate that, we propose to increase the RX intermediate frequency (IF) to just beyond the flicker corner frequency and filter the IF signal using complex-domain cascaded bandpass filters (BPFs). The first of filters is clocked at multiples of the LO frequency performing sufficient filtering and harmonic rejection. System-level aspects of the BLE DT-RX are beyond the scope of this paper and are discussed in [38].

The remainder of this paper is organized as follows. Section III gives an overview of the ULP aspects of ADPLL and TX and discusses the vertical RF integration of passive and

active components. Section IV details the DT-RX implementation. Section V reveals the RFIO matching and switching. In Section VI, the experimental results are discussed.

III. ALL-DIGITAL PHASE-LOCKED LOOP AND TRANSMITTER ARCHITECTURE

The LO signal for the BLE TX and RX is derived from a DCO running at 4.1–5.1 GHz (see Fig. 2). This promotes smaller on-chip transformers with maximized quality factor (Q). Two separate $\div 2$ dividers generate the required quadrature signals (CKV^{0-3} in Fig. 2) for the RX mixer and predictive TDC [23] that supports ADPLL locking for any crystal oscillator’s frequency reference (FREF) between 1 and 40 MHz. In the TX mode, the DPA feeds the RFIO pin with $P_{out} \leq 3$ dBm, which may be controlled in 16 steps ($-5 \dots 3$ dBm range with finer resolution at higher power levels [18]) to save power and to limit interference to other users. In this TRX IC chip, the Gaussian frequency shift keying (GFSK) modulating data are stored in SRAM.

For IoT applications, flexible power management is essential to improving the battery life. Several techniques are exploited here to reduce the TX power consumption. First, supply voltage reduction leads to significant power savings for RF critical circuits (i.e., oscillator and power amplifier) [18] and makes it more compatible with energy harvesters, e.g., photovoltaic cells. Nominal supply voltage for core devices in a 28-nm LP CMOS technology is 1.05 V but is projected to scale towards 0.5 V in several generations of FinFET technology. Second, a dynamically programmable reference clock is employed to scale down the ADPLL update rate from 40 MHz to 5 MHz. The ADPLL digital logic power consumption will benefit proportionally to the frequency down-scaling ratio, while the in-band PN (i.e., between 1 and 100 kHz) will deteriorate by the same amount. Last, after ADPLL is settled, the DCO can be put in an open-loop modulation for great savings in power consumption. However, if the dynamically reduced FREF rate or the open-loop DCO approach is to be used, the most important factor to be considered is system tolerance to the frequency drift, which must be well below the BLE limit of $400 \text{ Hz}/\mu s$ [11], [24]. Besides, as the CMOS technology is scaled down, the relative area occupied by on-chip transformers/inductors will be increasing because the transformers cannot scale down as does the minimum feature size of technology. In this paper, both DCO and DPA with active devices underneath the transformers are reported. This achieves a 30% area reduction compared with a previous design [18] using lateral separation of passives and actives.

Supported by the low flicker noise of the oscillator, the ADPLL first acquires the lock in closed loop and then freezes the DCO tuning words while mostly shutting itself down [i.e., only the red bold circuits in Figs. 2 and 3 are operational], letting the DCO to free-run and to generate the LO signal for TX (FM-modulated) and RX (CW) packets in open loop. Alternatively, the blue bold circuits in Fig. 2 allow the effective reference clock to be dynamically scaled down in the closed-loop operation to save digital power. For more details, see [18] and Section VI.

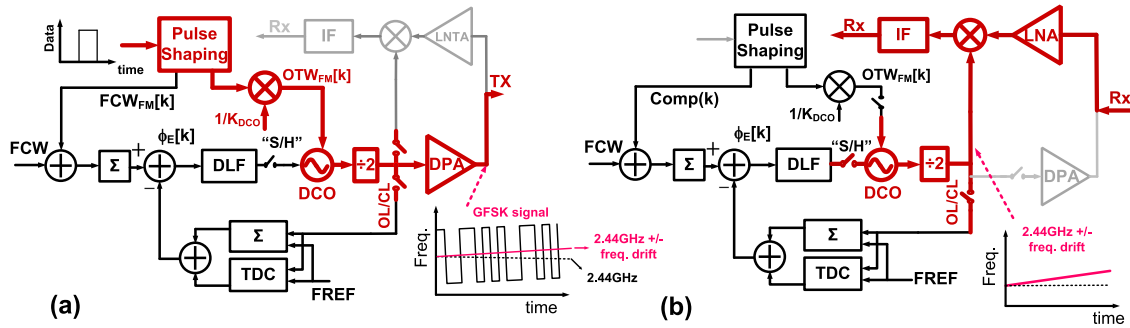


Fig. 3. Open-loop architecture. (a) TX mode. (b) RX mode. While the TX and the RX use separate $\div 2$ dividers, it is logically shown as the one here.

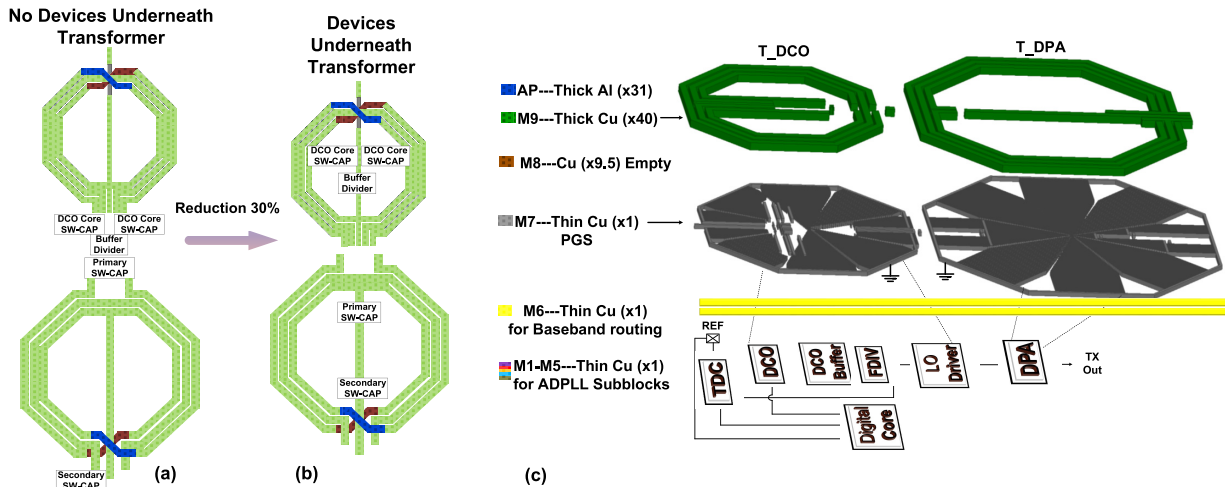


Fig. 4. Area comparison of TXs with transformer/inductor area-dominated oscillators and power amplifiers. (a) Traditional approach *with no* devices underneath transformers. (b) New approach *with* devices underneath transformers. (c) Conceptual multilayer metal arrangement for the vertically integrated TX with DCO and DPA transformers.

A. Vertical Layout Integration

The area of the proposed TX is dominated by two large passive components: a tuning LC tank transformer in the switched current-source DCO and a matching-network transformer in the class-E/ F_2 DPA. The DCO transformer needs to be optimized for the largest Q -factor possible in a given technology, since both its spot PN $\mathcal{L}(\Delta f)$ and figure of merit (FoM) are proportional to $1/Q^2$. Likewise, the Q -factor of the DPA transformer needs to be maximized to achieve the reasonably highest efficiency, $\eta_{p(max)}$, as derived in [25]

$$\eta_{p(max)} = \frac{1}{1 + \frac{2}{k_m^2 Q_p Q_s} (1 + \sqrt{1 + k_m^2 Q_p Q_s})} \quad (1)$$

where Q_p and Q_s are, respectively, the Q -factors of the DPA transformer's primary and secondary windings and k_m is the magnetic coupling factor between the windings.

Inspection of inductors available in this process design kit reveals that there exists a certain minimum area of an inductor below which its Q -factor starts dropping. Further, as shown in [26], at the same inductance value, multiturn windings occupy smaller area but have much lower Q -factor than with a single turn. We surmise that observation would extrapolate to transformers. This reasoning concludes that

further area reduction in the transformer-/inductor-dominated TX would only be possible by making the active devices (i.e., the remainder of the constituting components) somehow “disappear” beneath these passives [27]. Naturally, this needs to be done without degrading the precious Q -factor and other performance parameters.

Fig. 4 illustrates this idea of vertical integration. In a conventional TX layout implementation, such as that in [18], the circuitry associated with each of the two transformers is placed laterally nearby [see Fig. 4(a)]. In the proposed implementation, shown in Fig. 4(b), these associated components are placed *underneath* their respective transformers. Specifically, the DCO transformer shares its die area vertically with its cross-coupled transistors, switchable tuning capacitor banks, output buffer, and divider, whereas the DPA transformer shares its die area vertically with its clock network, switching transistors, and matching switchable-cap banks. This way, the 30% area reduction of the TX has been achieved with no detrimental effects to the performance, as will be explained in the following.

Fig. 4(c) reveals the vertical arrangement of the TX within the multilayer metal stackup. In this 28-nm digital CMOS technology, the upper Cu metal layers M8, M9, and AP are, respectively, $9.5\times$, $40\times$, and $31\times$ thicker than the thin

TABLE I
COMPARISON OF TRANSFORMER PARAMETERS FOR DCO AT 5 GHz, DPA AT 2.5 GHz

	Transformer Model Parameters	DCO,P	DCO,S	DPA,P	DPA,S
w/o PGS	$C_{OX}(fF)$	10.8	28	33	13
	$C_{SUB}(fF)$	12.3	12.3	12.3	12.3
	$R_{SUB}(k\Omega)$	4.15	1.5	1.28	3.9
w/i PGS	$C_{OX,m79}(fF)$	14.8	38	44.7	17.6
	$L_p, L_s(nH)$	0.36	1.045	1.41	0.43
	$C_p, C_s(fF)$	0.01	0.031	0.038	0.02
	$r_p, r_s(\Omega)$	1.71	3.6	3.9	1.85
	$C_c(fF)$	5.25	5.25	5.7	5.7
w/o PGS	Substrate Loss Factor (SLF)	0.55	0.54	0.53	0.554
	Q	12.8	15.1	15.9	11.4
	Self-resonant Frequency (GHz)	19.4	19	12.6	12.7
w/i PGS	Substrate Loss Factor (SLF)	0.96	0.957	0.929	0.97
	Q	12.9	15.6	16.8	11.4
	Self-resonant Frequency (GHz)	19.1	18.3	12.3	12.5

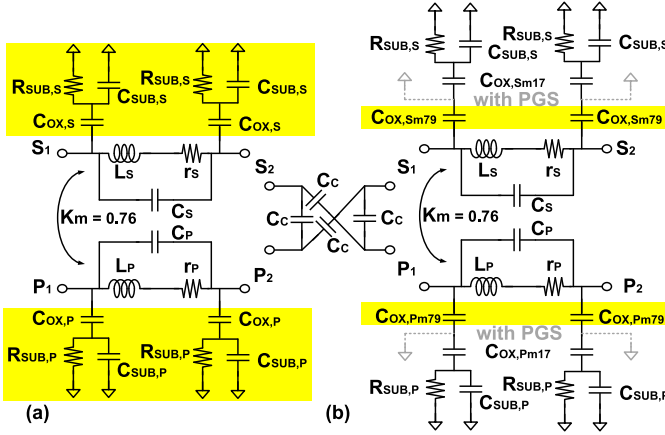


Fig. 5. Simplified model of on-chip transformer. (a) Without PGS. (b) With PGS.

lower Cu metal layers M1–M7 of uniform thickness (i.e., $1\times$). To obtain high-quality factors (e.g., $Q > 11$) at the resonance frequency, the two transformers (T_DCO and T_DPA) occupy the dedicated three upper thick-metal layers (M8–AP). The main coils are routed at M9, with M8 and AP serving only for cross routing. The core devices occupy metal layers M5 and lower, allowing placement underneath the transformers. A signal routing channel for non-RF signals is implemented at M6, which is largely kept empty but available to promote future integration. The patterned ground shield (PGS) implemented in M7 is placed between the transformers and the ADPLL/TX circuitry to improve isolation with “noisy” active circuitry at M1–M6. The optimal vertical integration arrangement was determined through extensive electromagnetic (ADSTM/PeakView LEMTM) simulations. Keeping M8 largely empty turned out to favorably reduce capacitance between M7 (PGS) and M9 (transformer).

To gain deeper understanding, Fig. 5(a) illustrates the simplified equivalent circuit of the transformer model without the PGS and is compared with that of the transformer model in

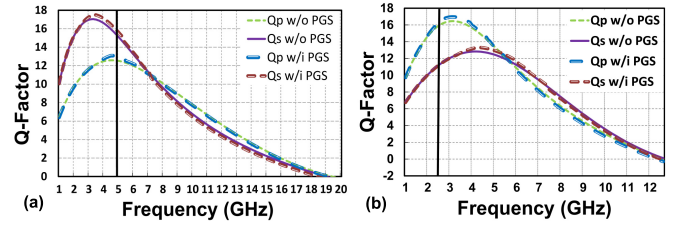


Fig. 6. Q -factor simulations of transformers with and without PGS. (a) DCO. (b) DPA.

Fig. 5(b) with the PGS. The overall Q -factor calculation of the transformer’s primary winding is given by (2), based on a method in [27]. The secondary winding inductance L_s can be analyzed similarly as

$$Q_p = \frac{\omega L_p}{r_p} \cdot \frac{R_X}{R_X + \left[\left(\frac{\omega L_p}{r_p} \right)^2 + 1 \right] \cdot r_p} = Q_{p,L} \cdot \text{substrate_loss_factor} \quad (2)$$

in which the equivalent parallel resistance R_X is

$$R_X = \frac{1}{\omega^2 \cdot C_{OX}^2 \cdot R_{sub}} + \frac{R_{sub}(C_{OX} + C_{sub})^2}{C_{OX}^2} \dots (\text{no PGS}) \quad (3)$$

$$R'_X \rightarrow \infty \dots (\text{with PGS}) \quad (4)$$

where L_p is the transformer’s primary winding inductance, r_p is its series metal resistance, C_{OX} is the thick-oxide capacitance, C_{sub} is the substrate capacitance, R_{sub} is the substrate resistance, and $C_{OX,m79}$ is the oxide capacitance between PGS (M7) and M9.

In Fig. 5, an impedance seen by the primary winding inductance L_p and presented by the combination of C_{OX} , C_{sub} , and R_{sub} is replaced by a parallel equivalent resistance R_X in (3), which is frequency dependent. However, when the PGS is added, this equivalent resistance becomes very large as R'_X in (4). This is shown in Fig. 5(b) as the PGS at M7 is

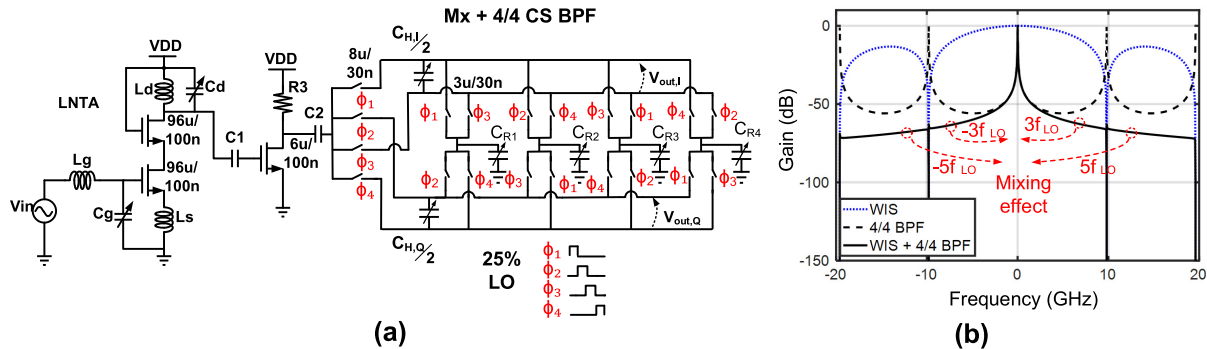


Fig. 7. (a) Full-rate RX strip. (b) TF of 4/4 CS-BPF also showing WIS.

shorted to ground, and C_{OX} , C_{sub} , and R_{sub} can be ignored, thus increasing the winding's Q -factor. However, M7 brings the bottom plate of the shunt parasitic capacitance closer to the inductor, which now appears as $C_{OX,m79}$ and which somewhat decreases the self-resonance frequency of the winding.

A comparison of the transformer's parameters obtained through EM simulations between the cases of "without PGS" and "with PGS" is shown in Table I. The results confirm that the transformer's substrate loss "with PGS" is lower than that of "without PGS" but at a cost of a bit lower self-resonant frequency.

Simulated Q of the transformers, shown in Fig. 6, further illustrates better Q -factors with the PGS than without the PGS in the operating frequencies of interest. This confirms that the insertion of PGS and use of proper empty layers (M8) will allow the same or better Q -factors compared with [18], while preventing any significant coupling from the TX sub-blocks underneath, as verified via performance measurements in Section VI. The peak Q_p and Q_s of resonator with the components underneath are ~ 17 and 13 , which are $\sim 3\%$ higher than ~ 16.5 and 12.5 of the transformer with the components outside, respectively.

IV. DISCRETE-TIME RECEIVER

Recent ULP RXs for BLE achieve significant power reduction [3], [28] and higher level of integration [5], [8], [10] primarily using sliding IF and low-IF continuous-time architectures. To simultaneously reduce the RX power consumption beyond state of the art while maintaining adequate performance margin with the stated goal of direct antenna connection (see Fig. 1: shared *single* TX/RX RFIO pin and no external RF components, such as bulky and costly antenna band-selection filter), we propose a DT high-IF or superheterodyne RX architecture with complex-signaling BPFs and a progressively reduced sampling rate. The approach exploits the charge-sharing (CS) BPF recently introduced for a high-performance cellular 4G RX [15], [16] and now adapted for the first time for ULP applications.

To be able to eliminate the external RF components, out-of-band (OOB) blockers are attenuated here using a combination of a charge-sampling mixer and a full-rate ($\sim 4 \times 2.45$ Gsamples/s) CS-BPF, which are protected from aliasing only by selectivity of a narrow-band LNTA. An additional OOB blocking protection margin is offered by the

fully integrated TX/RX matching network. The full-rate DT circuitry is followed by two cascaded CS-BPFs that operate at $16\times$ decimated sampling clocks for power reduction, thus preparing the received signal for moderate dynamic range and aliasing requirements of the following ADC.

A. Full-Rate Sampling Strip

The front-end section (strip) of DT-RX is presented in Fig. 7. It consists of the narrow-band LNTA, a single-ended-to-differential quadrature sampling mixer, and a DT 4/4 CS-BPF. The 4/4 CS-BPF is implemented with four rotating capacitors (C_R) sampled at four phases with 25% duty cycle (D).

There are two key principles here. First, with no interstage decimation, both the mixer and DT filter operate at the same effective sampling frequency, $4\times$ higher than LO ($f_s = 4f_{LO}$), giving an OSR of more than 2, which avoids aliasing up to the third clock harmonic. Second, the low quality factor (Q) of the complex 4/4 CS-BPF is mapped to a high Q of RF input filtering by means of frequency translation by the current-mode sampling mixer [29], [30]. This beneficial mixer transparency effect was first exploited for a CS-BPF architecture in a highly linear software-defined radio for cellular 4G applications [16]. For the ULP application designed here, the high-performance but power-hungry architecture composed of a differential LNTA, 8-phase sampling mixer, and 8/16 CS-BPF with harmonic rejection introduced in [16] is converted into an ULP structure. A single-ended narrow-band LNTA, a 25% duty-cycle quadrature passive mixer, and a 4/4 CS-BPF are presented in Fig. 7.

The LNTA is composed of two stages: a single-input/single-output common-source cascode low-noise amplifier (LNA) and a common-source transconductance (g_m) amplifier. Both stages operate in moderate inversion ($g_m/I_d = 18$ and 12 V^{-1}) as opposed to a strong inversion operation in prior reports, in order to reduce power consumption with $I_d = 400$ and $100 \mu\text{A}$, respectively, biased with current mirrors (not shown in Fig. 7). Capacitors C_g and C_d are 4-b programmable to tune the LNTA input matching network and its tank load over process, voltage, and temperature (PVT), as well as over package parasitics.

Besides converting from single-ended into differential, and hence implicitly acting as a balun, the $D = 25\%$ quadrature passive mixer operation results in a low quadrature imbalance, low noise, and high linearity [31]. The sampling mixer

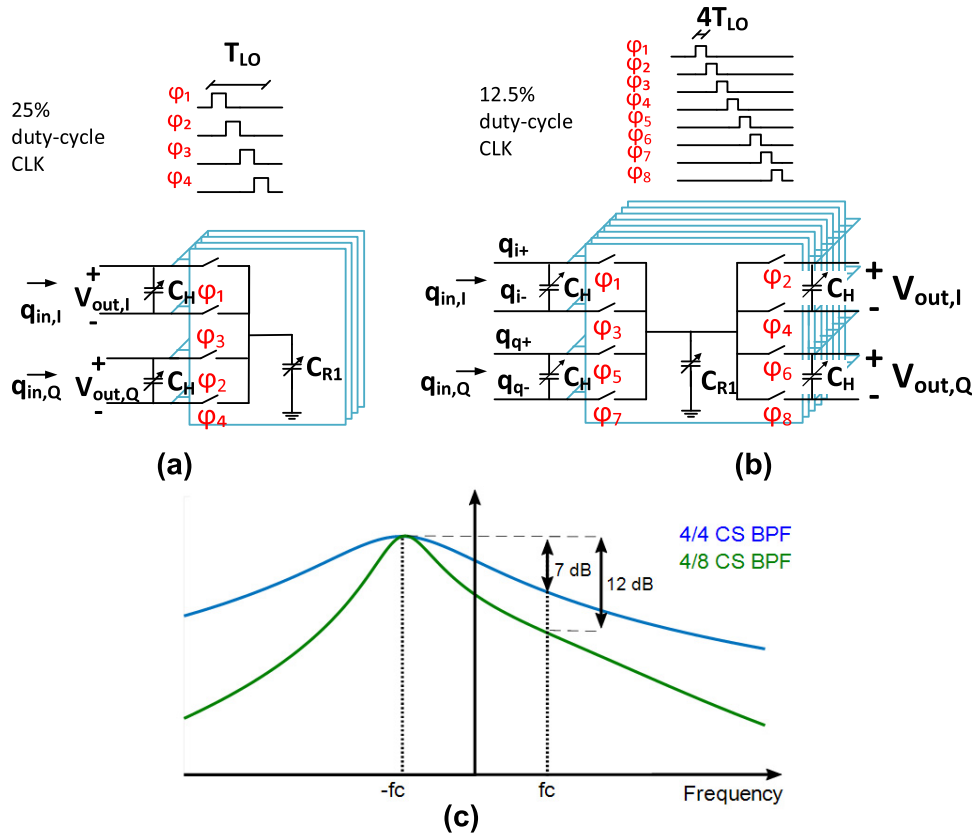


Fig. 8. (a) 4/4 CS-BPF filter schematic and signal waveforms. (b) 4/8 CS-BPF filter schematics and signal waveforms. (c) Comparison of 4/4 and 4/8 CS-BPF TFs.

with current-mode input/output is cascaded with the first complex BPF. Transfer function (TF) of the 4/4 CS-BPF in z -domain, from the charge input $Q_{in}(z)$ to the voltage output $V_{out}(z)$ is given by

$$H_{4/4 \text{ CS-BPF}}(z) = \frac{V_{out}(z)}{Q_{in}(z)} = \frac{1/(C_H + C_R)}{1 - [\alpha + j(1 - \alpha)]z^{-1}} \quad (5)$$

where C_R is the rotating capacitor, C_H is the history capacitor, and $\alpha = C_H/(C_H + C_R)$. Q -factor of the 4/4 CS-BPF is directly related to the output resistance of the previous cell (R_{out}). When $R_{out} \geq 3R_{eq}$, where R_{eq} is the input resistance of the filter, the best Q of 0.5 is obtained. R_{eq} and center frequency (f_c) of the filter are given by the following and offer a tradeoff between capacitor size (area), sampling frequency (power) and noise:

$$R_{eq} = \frac{1}{C_R f_s}, \quad f_c = \frac{f_s}{2\pi} \arctan\left(\frac{C_R}{C_H}\right). \quad (6)$$

The gain of the first stage is given simply by $G_m \times R_{eq}$, product of effective transconductance of LNTA and its resistive load, R_{eq} . In this ULP application, the strategy is to reduce C_R as much as possible in order to increase R_{eq} and, consequently, the gain of the first stage, reducing the overall noise figure (NF) of the full-rate strip. The LNTA output impedance is increased by designing the second-stage transistor with $L = 100$ nm, which results in $R_{out} = 3.5$ k Ω . Here, C_R was selected as 100 fF but a smaller C_R value would improve noise while reducing filter quality.

To reduce area, C_H capacitors are implemented differentially as its equivalent series $C_H/2$, as noted in Fig. 7. To account for PVT variations and offer flexibility in f_c tuning, C_H and C_R are implemented as 5-bit binary-weighted capacitor banks. The combined banks enable programming of f_c from 1 to 14 MHz and R_{eq} from 667 Ω to 4.67 k Ω .

Fig. 7(b) plots a TF of the infinite impulse response (IIR) filter of 4/4 CS-BPF (5). As expected of any DT filter, TF reveals repetition peaks (replicas) at multiples of f_s (≈ 9.8 GHz). Repetition peaks are folded to dc, but not before being attenuated by a windowed integration sampling (WIS) effect of the current-mode sampling, which creates an in-built sinc filter response, also shown on the plot. The combination of these two effects creates a filtering shape nearly independent of the repetition [32], [33]. Due to the mixing operation, odd harmonics of LO ($\pm 3f_{LO}$, $\pm 5f_{LO}$, ...) are also translated to dc after being attenuated by the 4/4 CS BPF with more than 60 dB of protective filtering. It should be noted that BLE requires protection from -35 dBm OOB blockers, which means 50 dB of attenuation to keep the RX SNR at ≥ 15 dB.

B. IF Filtering at Decimated Clock

The back-end strip of analog DT-RX conditions the IF signal for the 20-Msamples/s 9-bit SAR ADC. The pass-band IF signal is amplified while in-band interferers are sufficiently attenuated such that they do not saturate the ADC nor alias due to its sampling. This strip is composed of programmable inverter-like gain stages and two 4/8 CS-BPFs [16]. Schematics of both 4/4 and 4/8 CS-BPFs are shown in

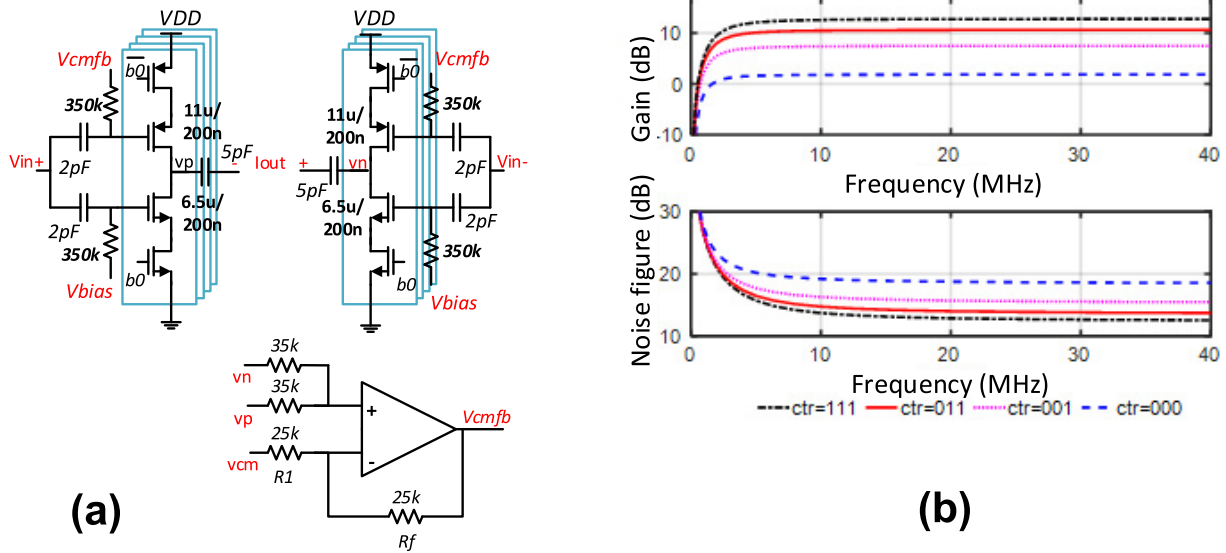


Fig. 9. (a) g_m cell schematics. (b) g_m cell gain and NF at various register setting levels.

Fig. 8(a) and (b), respectively. The 4/8 CS-BPF, as opposed to the 4/4 CS-BPF, is based on eight rotating capacitors sampled at eight phases with $D = 12.5\%$, which results in a quadrature filter with higher quality factor ($Q = 1.14$). The z -domain TF of charge input to voltage output is

$$H_{4/8 \text{ CS-BPF}}(z) = \frac{V_{out}(z)}{Q_{in}(z)} = \frac{1/(C_H + C_R)}{(1 - \alpha z^{-1})^2 - j[(1 - \alpha)z^{-1}]^2} \quad (7)$$

where $\alpha = C_H/(C_H + C_R)$. C_H and C_R are also implemented using 5-b programmable capacitor banks to allow for IF and input impedance adjustments. Fig. 8(c) compares TFs of both filters according to (5) and (7), showing 5 dB of extra image rejection improvement in the 4/8 CS-BPF case.

Since the 4/8 CS-BPF is composed of $4 \times$ more switches than its counterpart, it could suffer from higher power consumption. This effect is alleviated by clocking the filter at a reduced $\div 16$ rate. This decimation process is trivially implemented by clock reduction, allowing multiple input samples to be integrated onto the rotating capacitors creating a finite impulse response filter described by (8) [33], [34]

$$H(z) = \frac{1 - z^{-16}}{1 - z^{-1}} \Rightarrow |H(f)| = \left| \frac{\sin(\pi f 16/f_s)}{\sin(\pi f/f_s)} \right|. \quad (8)$$

Gain stages in the RX path are implemented using highly linear inverter-like transconductors presented in Fig. 9(a). Programmable gains of 1.7, 7.1, 10.5, and 12.5 dB are supported considering a load of $3.27 \text{ k}\Omega$ presented by the input resistance of the 4/8 CS BPF. In order to increase output impedance and produce current output, g_m stage devices are sized with $L = 200 \text{ nm}$. Fig. 9(b) presents gain and NF simulations for the programmable gains. g_m -cell inverters are biased in moderate inversion ($g_m/I_d = 18 \text{ V}^{-1}$) with a current of $12 \mu\text{A}$ to reduce power consumption. Biasing of pMOS devices is implemented using a common-mode feedback (CMFB) loop with 86° of phase margin. Input blocking capacitors at input and output of g_m -cells form high-pass

filters with bias resistors and CMFB resistors, respectively. The corner frequency of the resulting filter was designed at 1 MHz and can be observed in simulation results [Fig. 9(b)].

C. Clock Generation Circuitry

The $D = 25\%$ and 12.5% duty cycle clock phases needed for the DT-RX operation are generated in several steps. At first, a differential clock of $2f_{LO} \approx 4.9 \text{ GHz}$ from the DCO is divided by 2 to generate $D = 50\%$ quadrature clocks [Fig. 10(a)] using high-speed differential D-latches based on tri-state inverters designed with low- V_t devices [Fig. 10(b)]. In the second step, the $D = 50\%$ quadrature clocks are processed to generate $D = 25\%$ clocks, which are separately buffered for the mixer and 4/4 CS-BPF, using customized CMOS topologies with low- V_t devices, as presented in Fig. 10(c). Finally, the $D = 12.5\%$ clocks are generated using standard CMOS cells available in the technology and independently buffered for the two 4/8 CS-BPFs [Fig. 10(d)]. In order to minimize power consumption due to parasitic routing, the $D = 25\%$ generation blocks are located very close to the mixer and 4/4 BPF filter.

D. Strategies for Low-Power Discrete-Time Receiver Operation

The ULP operation achieved by this DT-RX is a consequence of a higher impedance of the DT filters and an aggressive clock decimation. In [15] and [16], the cellular DT-RXs feature a higher IF due to the required higher bandwidth and lower NF. Here, they work at $\text{IF} = 5 \text{ MHz}$, which is just beyond the flicker noise corner of active devices, and through (6), the capacitance C_R can be reduced with a consequent increase in input impedance of the filters (R_{eq}). Since the RX gains are of the form $G_m \times R_{eq}$, this increase enables high gain with lower g_m and hence with a lower current at the transconductors. The increase of the input impedances also allows for the use of smaller switches (with higher resistances) both in the mixer and in the filters, with a consequent

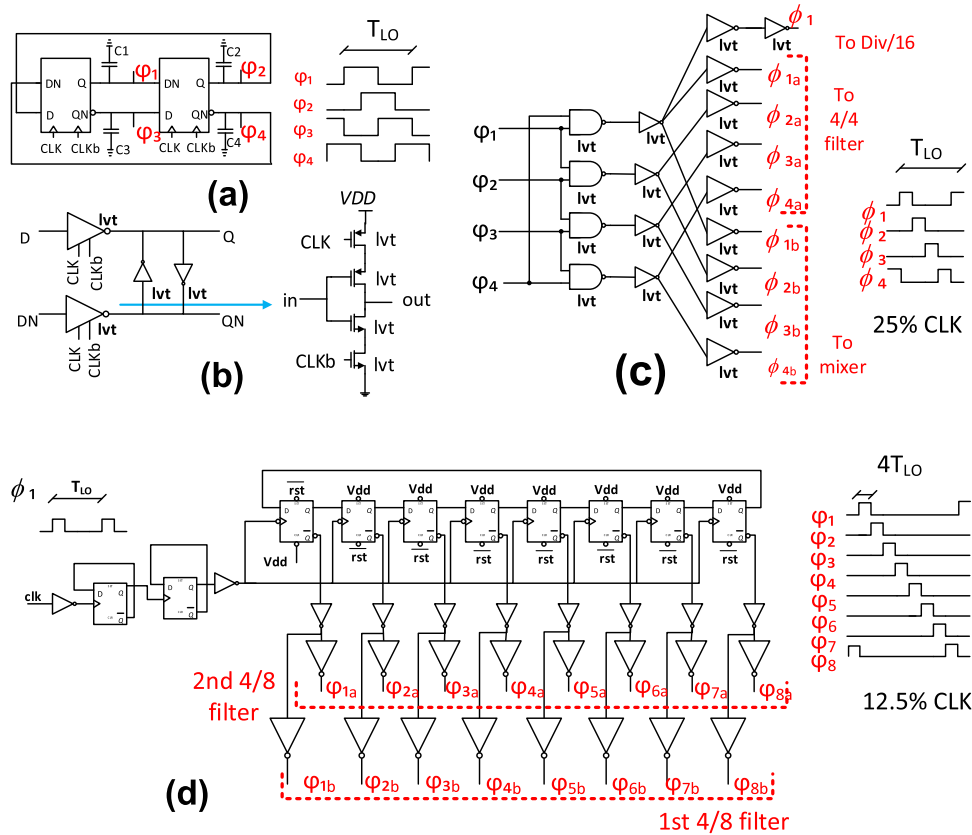


Fig. 10. (a) Generation of quadrature 50% duty cycle clocks. (b) High-speed latch implementation. (c) Generation of 25% duty cycle clocks. (d) Generation of 12.5% duty cycle clocks.

reduction in the power consumption of the clock generation. Additionally, the less challenging NF requirement of the BLE standard allows for the adoption of lower gain and power in the LNA, which ends up with a consequent increase of the LNTA output impedance. Consequently, it also beneficially allows for the increase in input impedance of the first filter, which must be around three times smaller than the LNTA's output impedance.

Relaxed linearity requirements of the BLE, especially when compared with [15] and [16], enables the LNA and g_m cells to work in moderate inversion, thus reducing power consumption of the g_m cell and LNA when compared with the alternative implementation of strong-inversion.

The next ULP technique is decimation, which is carried out as early as possible in the RX path. The first BPF stage runs at the full rate since it uses the same $4 \times f_{LO}$ sampling clock rate as that of the mixer. This is done to increase blocker protection and to reduce noise folding. The second BPF stage implements a decimation by 16 to drastically reduce power consumption of the clock generator. It is protected against aliasing by the first filter, which offers 55 dB (plus 13 dB due to the LNTA attenuation) of protection at a $4 \times f_{LO}/16 \approx 612.5$ -MHz offset, which is enough to avoid any impact on the RX sensitivity from folding of a blocker at that frequency [Fig. 7(b)]. From the standard requirements, the protection should be higher than $58 \text{ dB} = -30 \text{ dBm}$ (OOB blocker) + 67 dBm (required sensitivity) + 21 dB (co-channel interference defined by the

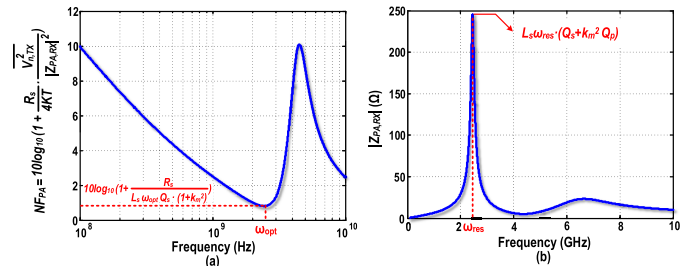


Fig. 11. (a) TX contribution to the NF of the system and (b) its output impedance in the RX mode. Conditions: $Q_p = 15$, $Q_s = 10$, $k_m = 0.75$, $n = 0.5$, $L_s = 880 \text{ pH}$, $C_1 = 0.5 \text{ pF}$, and $f_0 = 2.45 \text{ GHz}$.

standard) [11]. A decimation higher than 16 in the second stage would leave little margin for the filter implementation. Between the second and third filter stages, there is no further decimation in order to avoid any additional clock generation circuitry since the power consumption of these blocks is already very low (around $160 \mu\text{A}$ in simulations for both 4/8 CS-BPFs' clock generation, including buffers).

V. RADIO-FREQUENCY INPUT-OUTPUT SWITCHING AND MATCHING

Fig. 12(a) illustrates the proposed implementation of the on-chip matching networks with a *soft* T/R switch (i.e., without any explicit switches carrying RF signals) between the TX and RX paths. In the RX mode [see Fig. 12(b)], the PA transistors are OFF and, consequently, the TX is simplified to the PA

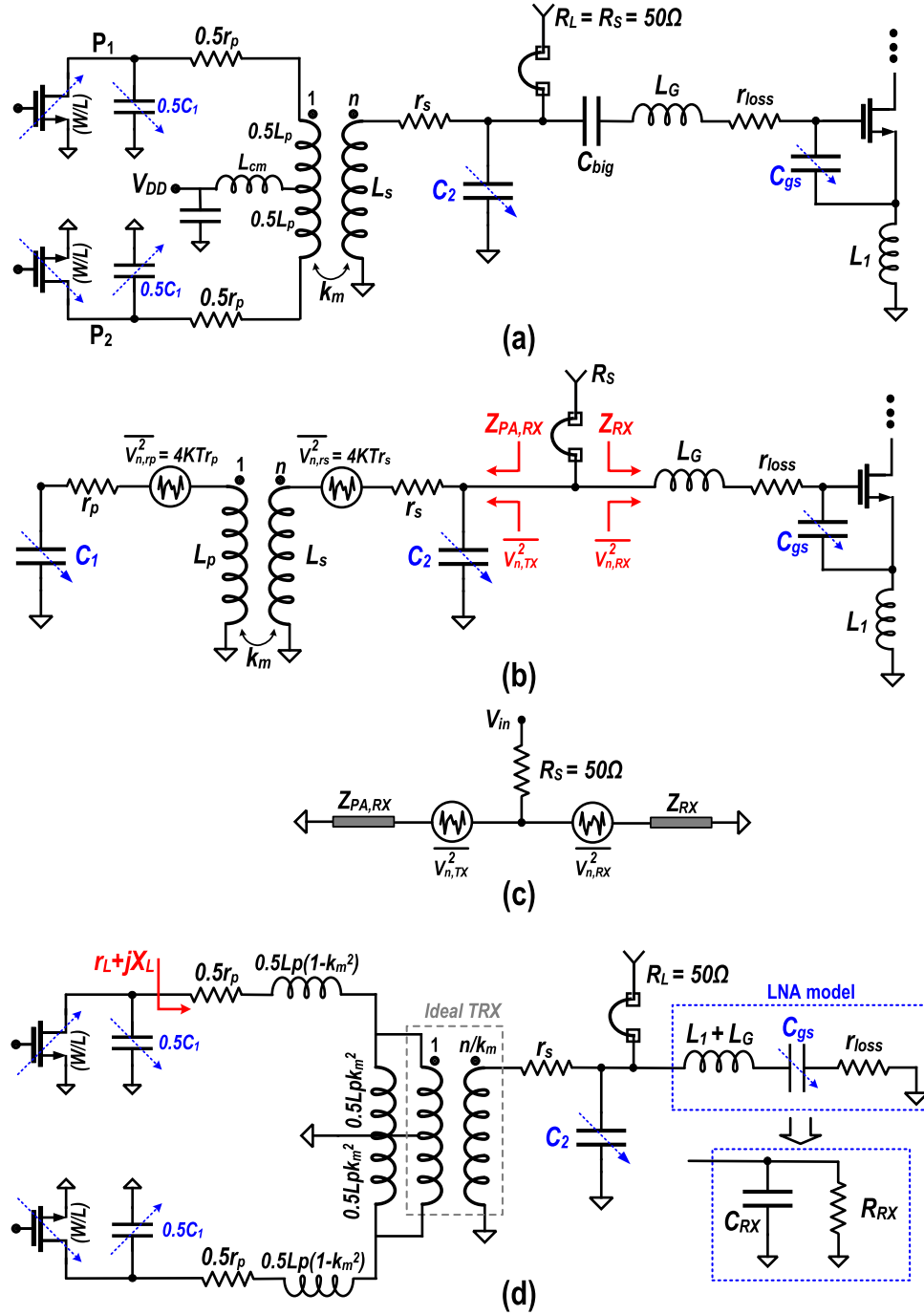


Fig. 12. (a) RFIO block including the first stage of LNTA and the last stage of class-E/F₂ PA. (b) RFIO in the RX mode. (c) Simplified circuit model for calculation of the NF of the RX. (d) RFIO in the TX mode.

transformer-based TX matching network (TXMN) acting as a second-order resonator. In this mode, the ultimate goal is to alleviate the side effects of TXMN on the RX NF and input return loss. To analyze the system in the RX mode, the Thevenin equivalent circuits of the TXMN and LNA are employed as shown in Fig. 12(c). The RX noise factor (F) can be calculated by

$$F = 1 + \frac{R_S}{4KT} \cdot \frac{\overline{V_{n,RX}^2}}{|Z_{RX}|^2} + \frac{R_S}{4KT} \cdot \frac{\overline{V_{n,TX}^2}}{|Z_{PA,RX}|^2} \quad (9)$$

where $\overline{V_{n,RX}^2}$ and Z_{RX} are, respectively, the equivalent input noise and input impedance of LNTA at the operating frequency ω_0 and may be estimated by the following equations [35]:

$$Z_{RX} = r_{loss} + \frac{g_m L_1}{C_{gs}} + \left((L_G + L_1) \cdot s + \frac{1}{C_{gs} \cdot s} \right) \xrightarrow{\omega_0 = 1/\sqrt{C_{gs} \cdot (L_G + L_1)}} Z_{RX} = r_{loss} + \frac{g_m L_1}{C_{gs}} \quad (10)$$

and

$$\overline{V_{n,RX}^2} = 4KT[r_{loss} + \gamma g_m \cdot (L_1 \omega_0)^2]. \quad (11)$$

Furthermore, $Z_{PA,RX}$ and $\overline{V_{n,TX}^2}$ are, respectively, the output impedance and equivalent output noise of the PA's matching network and may be calculated by (12) and (13), as shown at the bottom of this page, where k_m is the magnetic coupling factor of the transformer and r_p and r_s model the equivalent series resistance of the primary L_p and secondary L_s inductances [36]. To reduce the side effect of TXMN on the RX's noise factor, the last term in (9) should be minimized. By employing (12) and (13), then substituting r_p and r_s with $L_p\omega/Q_p$ and $L_s\omega/Q_s$, respectively, and assuming $Q_p Q_s \gg 1$, we obtain

$$\frac{\overline{V_{n,TX}^2}}{|Z_{PA,RX}|^2} = \frac{4KT}{L_s\omega Q_s} \cdot \frac{\frac{Q_s k_m^2 L_p^2 C_1^2 \omega^4 + (1 - L_p C_1 \omega^2)^2}{\frac{1}{Q_s^2} \cdot \left(1 - L_p C_1 \omega^2 \left(1 + \frac{Q_s}{Q_p}\right)\right)^2 + (1 - L_p C_1 \omega^2 (1 - k_m^2))^2}}{.} \quad (14)$$

As shown in Fig. 11(a), there exists a global optimum frequency ω_{opt} that minimizes the contribution of TXMN to the system NF. It can be shown that (14) reaches its minimum at

$$\omega_{opt}^2 \approx \frac{1}{L_p C_1} \cdot \frac{Q_p}{Q_p + Q_s}. \quad (15)$$

To achieve the minimum NF penalty, one should tune C_1 switchable capacitor to roughly adjust ω_{opt} to near ω_0 . The optimum $\overline{V_{n,TX}^2}/|Z_{PA,RX}|^2$ is then obtained by inserting (15) into (14)

$$\left(\frac{\overline{V_{n,TX}^2}}{|Z_{PA,RX}|^2}\right)_{\min} = \frac{4KT}{L_s\omega Q_s} \cdot \frac{k_m^2 Q_p Q_s + Q_s^2}{(Q_s + k_m^2 Q_p)^2} \xrightarrow{Q_p=Q_s} \left(\frac{\overline{V_{n,TX}^2}}{|Z_{PA,RX}|^2}\right)_{\min} = \frac{4KT}{L_s\omega Q_s (1 + k_m^2)}. \quad (16)$$

As a result, the noise factor penalty reduces with increasing Q_s and k_m , which fortunately coincides with efforts to optimize the efficiency of the PA's matching network [18]. However, a step-down transformer must be employed for the PA's matching network to scale up the load resistance seen by PA's transistor in order to achieve the highest possible efficiency at a relatively low output power of 3 dBm. It is

against the noise factor optimization, as evident from (16) and clearly demonstrates a tradeoff between TX efficiency and RX noise factor. The total noise factor may be estimated by inserting (10), (11), and (16) into (9)

$$F = 1 + \frac{r_{loss}}{R_s} + \gamma g_m R_s \left(\frac{L_1 \omega_0}{R_s}\right)^2 + \frac{R_s}{L_s \omega Q_s (1 + k_m^2)}. \quad (17)$$

By considering $L_s = 880$ pH, $Q_s = 11$, and $k_m = 0.75$, the noise factor penalty in (17) can be as low as 0.22.

On the other hand, the input impedance of the RX must be matched to the antenna impedance. The input matching of LNTA is quite sensitive to the imaginary part of the impedance seen from the output pad toward TX. Hence, it is desired that the main resonant frequency of PA's matching network is roughly adjusted at the operating frequency, ω_0 . It also facilitates designing the PA and LNTA more independently. The fundamental resonant frequency of the transformer-based resonator may be estimated by [36]

$$\omega_{res}^2 = \frac{1}{L_p C_1 + L_s C_2}. \quad (18)$$

Note that $L_p C_1$ should be chosen to satisfy (15) in order to achieve the lowest noise factor. Consequently, one should tune the switchable capacitors C_2 to adjust the PA's matching network resonant frequency at ω_0 . By inserting (15) into (18), we obtain

$$C_2 = \frac{1}{L_s \omega_0^2} \cdot \frac{Q_s}{Q_p + Q_s}. \quad (19)$$

Consequently, to simultaneously achieve the lowest NF and input insertion loss, one should adjust C_1 and C_2 switchable capacitors to satisfy (15) and (19), respectively. Under this condition, the TX's output impedance becomes purely resistive [see Fig. 11(b)] and may be estimated by

$$R_{PA,RX} = L_s \omega_0 Q_s \cdot \left(1 + k_m^2 \frac{Q_p}{Q_s}\right). \quad (20)$$

As a result, the input matching can be realized by adjusting the transconductance gain of LNTA via

$$g_m = \frac{C_{gs}}{L_1} \cdot \left(\frac{R_{PA,RX} \cdot R_s}{R_{PA,RX} - R_s} - r_{loss}\right). \quad (21)$$

Now, moving attention to the TX mode, the LNTA's transistor is OFF, and consequently, the RX path can be simplified to a series RLC network (RXMN) as shown in Fig. 12(d). In this mode, the ultimate goal is to alleviate the side effects

$$Z_{PA,RX} = \frac{s^3(L_p L_s C_1 (1 - k_m^2)) + s^2(C_1(L_s r_p + L_p r_s)) + s(L_s + r_s r_p C_1) + r_s}{s^4(L_p L_s C_1 C_2 (1 - k_m^2)) + s^3(C_1 C_2(L_s r_p + L_p r_s)) + s^2(L_p C_1 + L_s C_2 + r_p r_s C_1 C_2) + s(r_p C_1 + r_s C_2) + 1} \quad (12)$$

$$\overline{V_{n,TX}^2} = 4KT \cdot \frac{r_p |k_m^2 L_p L_s C_1^2 s^4| + r_s \cdot |1 + r_p C_1 s + L_p C_1 s^2|^2}{|s^4(L_p L_s C_1 C_2 (1 - k_m^2)) + s^3(C_1 C_2(L_s r_p + L_p r_s)) + s^2(L_p C_1 + L_s C_2 + r_p r_s C_1 C_2) + s(r_p C_1 + r_s C_2) + 1|^2} \quad (13)$$

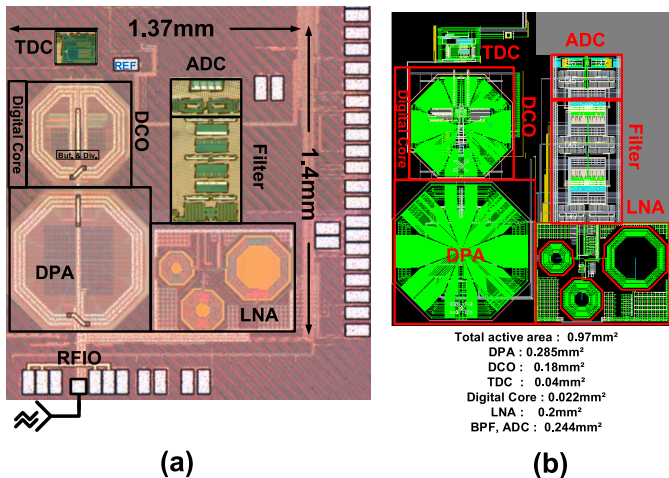


Fig. 13. Die micrograph of the proposed BLE transceiver (a); its layout with breakdown of subblock areas (b).

of RXMN on the efficiency of the PA. To analyze this efficiency drop, it is more convenient to replace the RLC series network with its equivalent parallel capacitance (C_{RX}) and resistance (R_{RX}), as illustrated in Fig. 12(d). It can be shown that

$$R_{RX} = r_{\text{loss}} \cdot \left(1 + Q_{RX}^2 \cdot \left(\frac{\omega_{RX}}{\omega_0} - \frac{\omega_0}{\omega_{RX}} \right)^2 \right) \quad (22)$$

and

$$C_{RX} = C_{gs} \cdot \frac{Q_{RX}^2 \cdot \left(\left(\frac{\omega_{RX}}{\omega_0} \right)^2 - 1 \right)}{1 + Q_{RX}^2 \cdot \left(\frac{\omega_{RX}}{\omega_0} - \frac{\omega_0}{\omega_{RX}} \right)^2} \quad (23)$$

where ω_{RX} and Q_{RX} are, respectively, the RXMN's resonant frequency $1/(L_1 + L_G)C_{gs}^{1/2}$ and its quality factor. Due to R_{RX} power dissipation, the PA's efficiency scales down with

$$\eta_{RX} = \frac{R_{RX}}{R_L + R_{RX}}. \quad (24)$$

As a result, the side effect of RXMN on the TX efficiency can be minimized by having a larger R_{RX} . As can be gathered from (22), this can be achieved by pushing the resonant frequency of LNTA's matching network to a much lower or higher frequency than ω_0 via the C_{gs} switchable capacitor bank. By simultaneously considering η_{RX} optimization over PVT variations and the quality factor degradation of switchable capacitors in an on-state, $C_{gs,\text{max}}/C_{gs,\text{min}}$ is chosen ~ 4 , resulting in $1.5 \text{ GHz} \leq \omega_{RX}/2\pi \leq 3 \text{ GHz}$. At the lower boundary of ω_{RX} , the PA sees the RX path as a small negative capacitor in parallel with $R_{RX} \approx 1\text{-k}\Omega$ modeling LNTA matching network losses. This negative capacitance is absorbed by the PA's matching network while R_{RX} creates a large resistance path for the TX signal (compared with the $50\text{-}\Omega$ load), which leads to a negligible penalty ($<5\%$) in the efficiency of the TX.

In the TX mode, the highest efficiency is achieved by adjusting the switchable C_{gs} to its maximum value and then tuning the C_1 and C_2 capacitors to satisfy the required matching network of class-E/ F_2 operation. As explained in depth in [18], class-E/ F_2 tuning exhibits the lowest systematic drain current and thus P_{out} at the same V_{DD} and load resistance among various flavors of differential switched-mode PAs. Consequently, this PA needs a smaller impedance transformation ratio for $P_{\text{out}} \leq 3 \text{ dBm}$, which results in a lower insertion loss for its matching network and thus higher system efficiency.

VI. EXPERIMENTAL RESULTS

Fig. 13(a) shows the die photo of the proposed TRX implemented in TSMC 1P9M 28-nm digital CMOS. The total core area, including empty space between the sub-blocks, is merely 1.9 mm^2 . Fig. 13(b) shows the corresponding layout with area breakdown of the constituting blocks, which totals 0.97 mm^2 . To save mask costs, only core devices are used with an exception of 1.05 V , 28-nm low- V_T (250 mV) transistors.

Fig. 14(a) plots a representative PN at fractional- N BLE channels. When used as an LO at F_{REF} down-divided to 5 MHz, the closed-loop ADPLL consumes 1.4 mW with an integrated PN of 1.06° . It exhibits in-band PN of -92 dBc/Hz , which corresponds to an average TDC resolution of $\sim 12 \text{ ps}$. Fig. 14(b) shows the ADPLL in-band PN at a 10-kHz offset, its PN performance at a 1-MHz offset, and oscillator's FoM^1 across ADPLL tuning range (TR) of 2.05–2.55 GHz. The oscillator's average FoM is 188 dB and varies $\sim 2 \text{ dB}$ across the TR. Moreover, the average in-band PN is -92 dBc/Hz with a 1-dB variation across the TR. The reason the input reference clock is divided down from 40 to 5 MHz, despite the $10 \log_{10}(40/5) = 9\text{-dB}$ in-band PN degradation, is to save the digital power of the ADPLL by 85%, as indicated in Fig. 14(c).

To achieve simultaneous fast locking and power savings, the loop bandwidth is dynamically controlled via a gear-shift technique [37]. During frequency acquisition, the loop operates in type-I, with a wide bandwidth of 2 MHz. It is then switched to type-II fourth-order IIR filter with a 500-kHz loop bandwidth when it enters the tracking mode. Finally, the loop bandwidth is reduced to 200 kHz to optimize the ADPLL integrated jitter. The measured lock-in time is $< 15 \mu\text{s}$ for f_{REF} of 5 MHz, as shown in Fig. 16(a). After the settling, the rest of ADPLL can be frozen (shut down) to improve power efficiency of the BLE TX and/or RX.

Fig. 15 verifies the 1.0-Mb/s GFSK modulation of the TX. Fig. 15(a) and (b) shows the measured eye pattern and modulation spectrum, without any intentional disturbances, e.g., on the supply line, at the midrange BLE channel of 2.456 GHz by a Rohde & Schwarz (R&S) vector signal analyzer. The measured GFSK modulation deviation for a 11110000 data pattern [i.e., without any intersymbol interference (ISI), which also corresponds to Δf_1 in the BT standard] over the entire BLE range is shown in Fig. 15(c). This measurement was retaken at 2.456 GHz for four IC samples and shown in Fig. 15(d). The average Δf_1 frequency deviation is 250 kHz (versus the specification of 225–275 kHz) and the

¹ $\text{FoM} = |\text{PN}(\Delta\omega)| + 20 \log_{10}(\omega_0/\Delta\omega) - 10 \log_{10}(P_{\text{DC}}/1\text{mW})$.

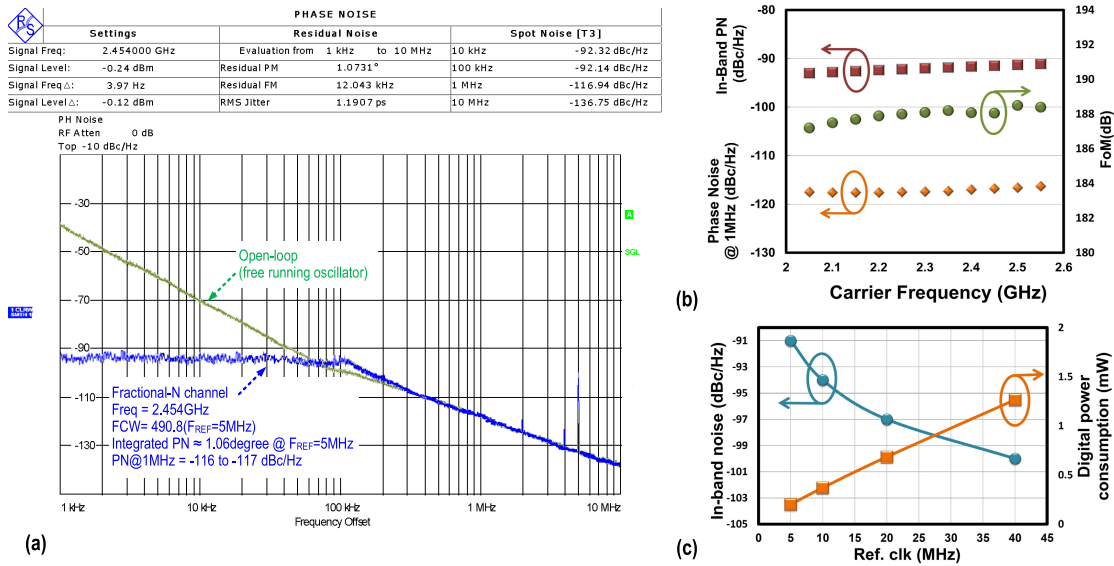


Fig. 14. Measured PN of the closed-loop ADPLL at 5 MHz FREF: (a) at a fractional-N channel with superimposed open-loop DCO; (b) PN, FoM at 1 MHz, in-band PN at 10kHz versus carrier frequency; (c) in-band PN, digital power consumption, versus various reference clocks.

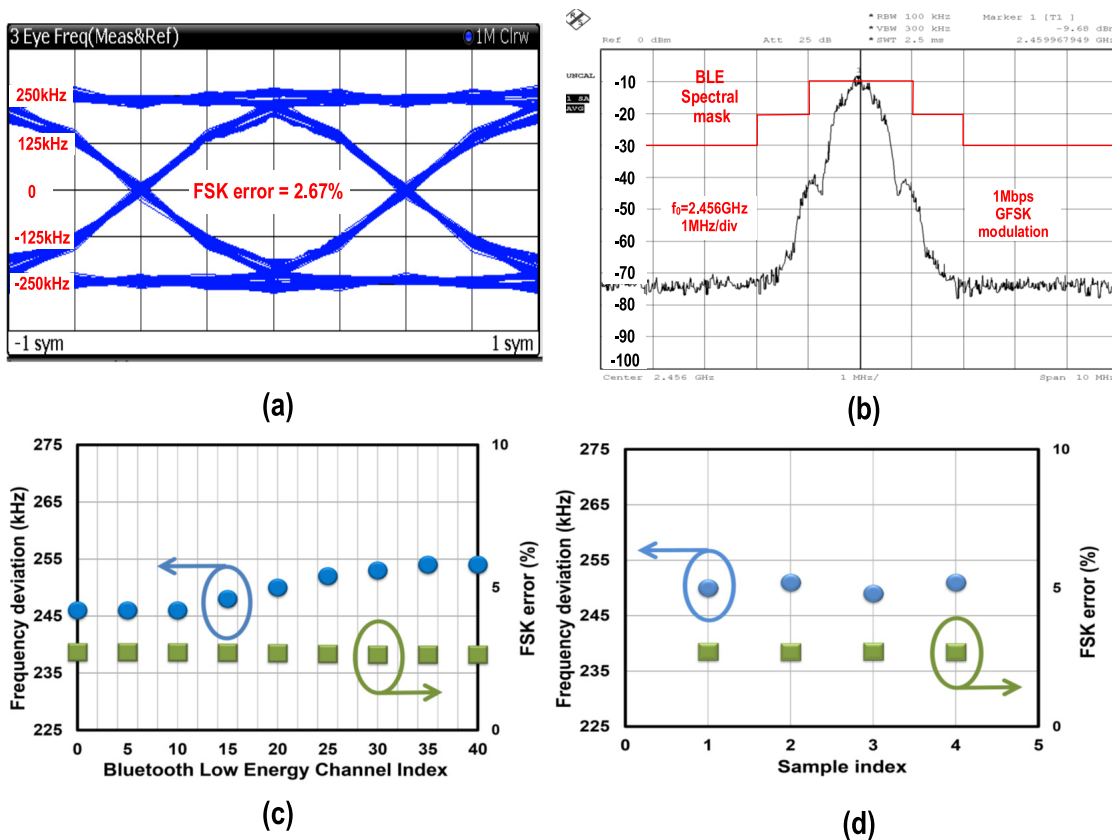


Fig. 15. Measured results for 1.0-Mb/s GFSK modulation: (a) FSK error at 2.456GHz; (b) GFSK output signal spectrum at 2.456GHz; (c) summarized modulation quality for carrier frequencies from 2.4 GHz to 2.48 GHz; (d) summarized modulation quality of multiple IC samples. Note that no disturbance has been applied during the measurements. Also note that the FSK error is defined as an average rms spread of the FSK demodulated symbol-spaced waveform around the ideal symbol locations.

worst-case RMS FSK error is less than 3%. Similarly, the average measured modulation deviation Δf_2 corresponding to the alternating “10” data pattern, which creates the most ISI

is 220 kHz [Fig. 16(a)]. This is close to a theoretical value with an ideal modulation. It leaves a 35-kHz margin above the 185-kHz specification, which needs to be 3σ , i.e., standard

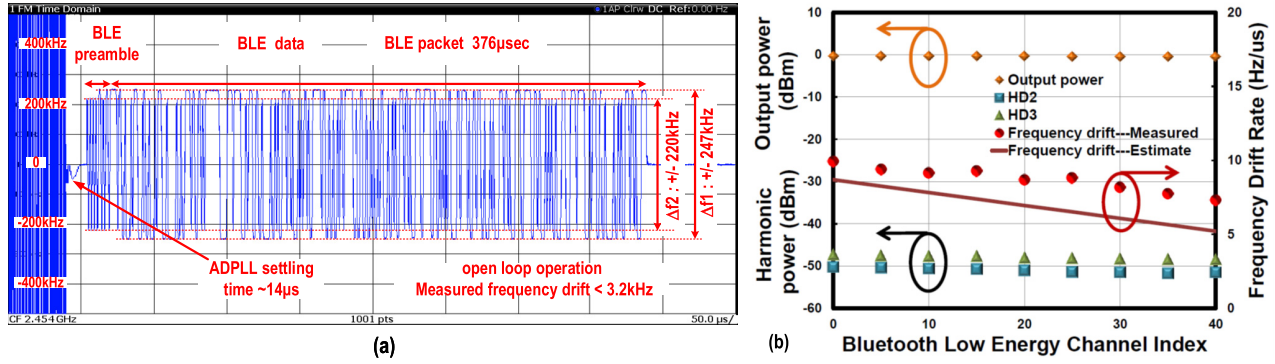


Fig. 16. (a) Demodulated TX frequency for 376µs BLE packet and its frequency deviation in the open-loop operation; (b) TX output power and harmonic power levels, frequency drift rate versus BLE channel index.

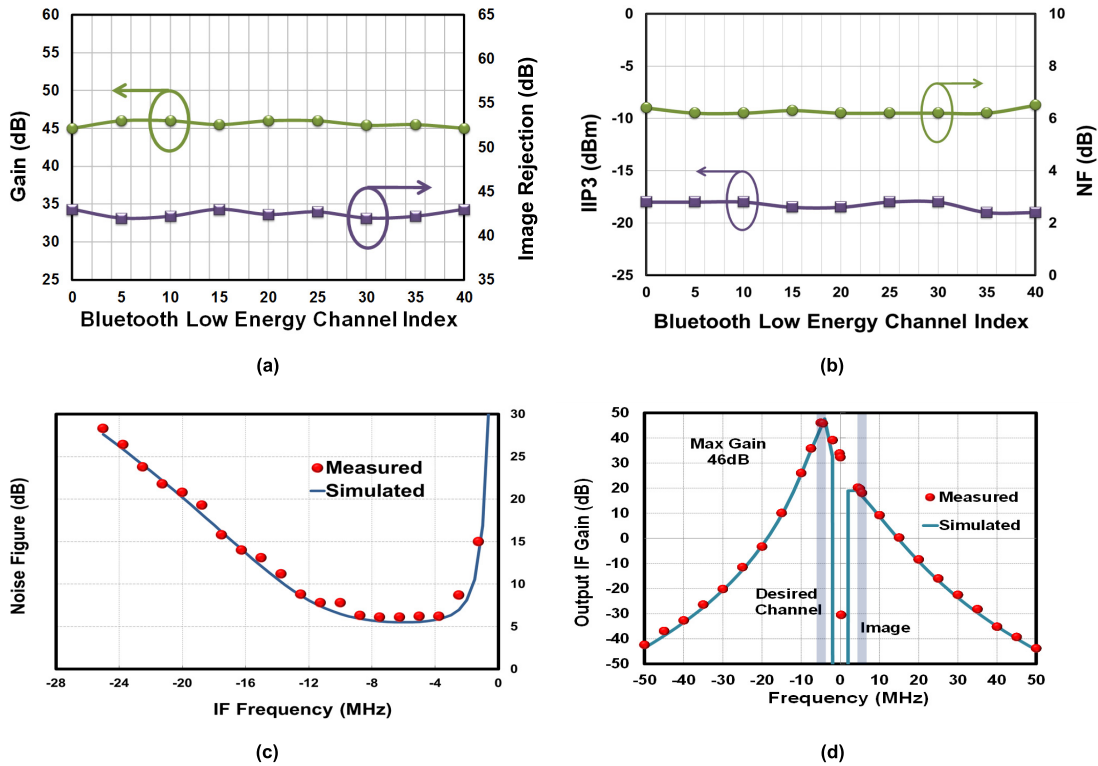


Fig. 17. Summary of the RX measurements: (a) gain and image rejection; (b) IIP3 and NF vs. BLE channel; (c) Noise figure of the RX at various IF frequencies; (d) RX filtering characteristics.

deviations (as dictated by the 99.9% probability requirement of the BLE specification) of the rms frequency noise.²

The maximum frequency drift between the 0/1 symbol at the start of the BLE packet and the 0/1 symbols at any-time within the packet payload shall be less than ± 50 kHz. Fig. 16(a) shows that it is properly satisfied here with ample margin even while in the open-loop operation. Thanks to the DCO's low flicker PN and frequency pushing, its frequency drift is extremely small. The Δf_1 frequency deviation here is ± 247 kHz and the worst case frequency drift is less than 8.5 Hz/µs within a single packet of 376 µs. We believe this technique can also handle multiple concatenated packets in the

² σ is calculated ~ 3 kHz from (25) and (26), which leaves enough margin.

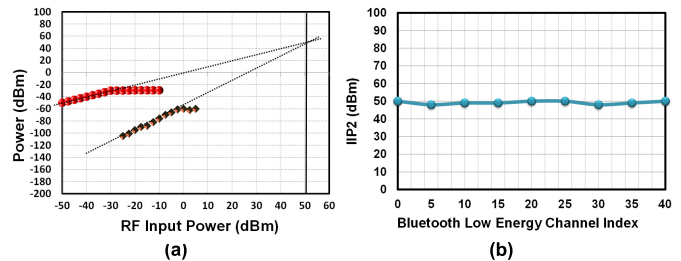


Fig. 18. Typical OOB IIP2 measurement (a), and IIP2 vs. BLE channel (b).

just-released BLE version 5, which extends its packet length to as long as 17 ms. Under this condition, the oscillator's residual FM noise due to its lowest frequency components

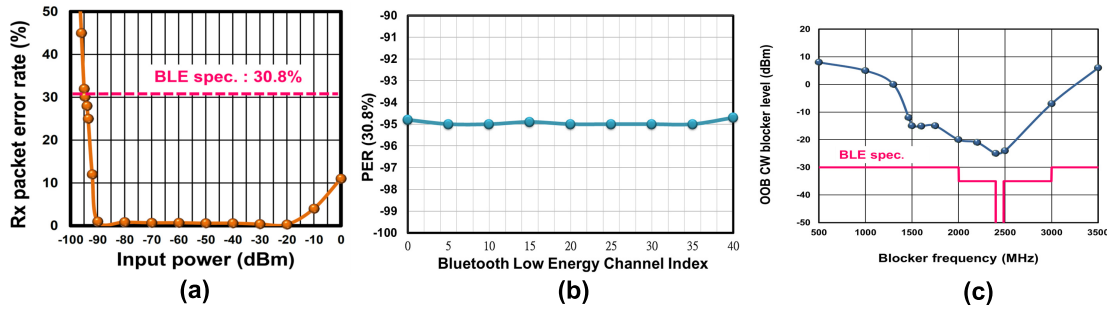


Fig. 19. BLE RX sensitivity measurement: (a) across input power at channel 40; (b) across BLE channel index; (c) OOB blocking performance.

($\ll 1$ MHz) together with its frequency drift due to voltage and temperature variations should be safely less than ± 50 kHz to satisfy requirements for the open-loop operation of a BLE TX. The oscillator's residual FM can be calculated by

$$\Delta f_{FM} = \sqrt{2 \int_{f_a}^{f_b} (\Delta f)^2 \cdot \mathcal{L}(\Delta f) \cdot d(\Delta f)} \quad (25)$$

where $\mathcal{L}(\Delta f)$ is the oscillator's PN at the offset frequency of Δf from the carrier. The lower integration bound f_a is inversely proportional to the BLE packet length (50 Hz for BLE 5, worst case). f_b is the bandwidth of the postdemodulation low-pass filter typically set a bit higher than the FSK symbol rate (i.e., 1 MHz). The PN of the proposed oscillator was reported in [18]. Its $1/f^3$ PN corner is ~ 100 kHz and its PN is -116 dBc/Hz at the 1-MHz offset from the carrier. Consequently, the oscillator's PN can be expressed by

$$\mathcal{L}(\Delta f) = \frac{2 \cdot 10^5}{(\Delta f)^3} + \frac{2}{(\Delta f)^2}. \quad (26)$$

As a result, the residual FM, Δf_{FM} , will be ~ 3 kHz. The PN of the proposed oscillator, therefore, appears to be good enough even for the 17-ms length of future BLE. On the other hand, as reported in [18], the frequency drift of the proposed oscillator is ~ 10.5 kHz during 3.4 ms of open-loop operation. By extrapolating the measured result, the frequency drift would be ~ 50 kHz for the 17-ms BLE packet, which meets the specification, but with no margin left. Hence, the voltage and temperature related drift components must be reduced in future implementations in order to operate in the open-loop mode for such a long packet.

The average second and third harmonic levels are -51 and -48 dBm, respectively. The harmonic levels remain well below the -41 dBm regulatory limit and are plotted in Fig. 16(b).

Functionality of the RX was verified on several channels covering the complete BLE band. Fig. 17(a) shows that the RX average performance figures are 46 dB of gain and >42 dB of image rejection (versus the BLE requirement of 31 dB). The finite image rejection is due to an uncompensated mismatch between I and Q clock phases. With no such imperfection, the rejection should be theoretically infinite for a superheterodyne RX [16]. Fig. 17(b) shows the average 6.5 dB of NF and -19 dBm of IIP3 from the first to the last BLE channel. The measured RX NF and filter characteristics are plotted

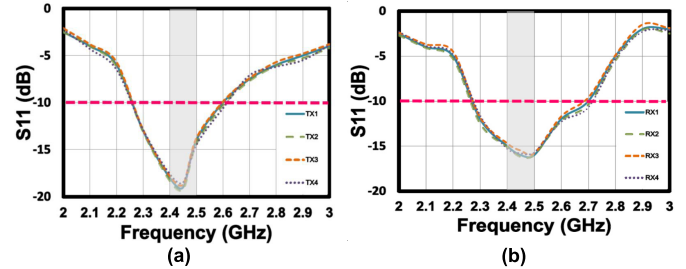


Fig. 20. Measured return loss in TX (a), and RX (b) modes over 4 IC samples.

in Fig. 17(c) and (d) and demonstrate excellent correlation with simulations using a linear PSS model. The NF variation is less than 1 dB for various IF offsets. Fig. 17(d) shows a gain of 46 dB at the -5 MHz IF with an image attenuation of 26 dB at $f_{LO} + 5$ MHz.

The OOB IIP2 of 50 dBm was measured for several channels in the BLE band in a two-tone test with frequencies 2.5 and 2.505 GHz. Typical IIP2 measurement curve and variations over BLE channels are presented in Fig. 18(a) and (b).

Fig. 19(a) shows the BLE RX packet error rate (PER) versus the input signal power. It was measured using an R&S CBTgo BT tester with help from an R&S FSW signal analyzer and a signal generator. The sensitivity is -95 dBm at 30.8% PER. Fig. 19(b) reveals merely a 1-dB sensitivity variation (under $PER \leq 30.8\%$) across BLE channels. For the OOB blocking measurement shown in Fig. 19(c), the desired BLE signal is fixed at channel 12 with an input power of -67 dBm. Both the desired signal and OOB CW blocker are injected into the RX. The OOB blocker power is recorded when the PER reaches 30.8%. The results corroborate with the proposed full-rate DT-RX strategy and show that the RX is able to tolerate the OOB BLE blocker mask shown in Fig. 19(c), thus eliminating the need for an expensive surface acoustic wave (SAW) or ceramic filter.

Fig. 20 shows the TRX's RF port matching in both modes of operation. In the RX mode, the return loss S_{11} is below -15 dB across the ISM band of 2400–2483.5 MHz, while in the TX mode it is between -19 and -13 dB.

The power consumption is summarized in Fig. 21. The supply voltage for the DCO and DPA is 0.5 V, while it is 1.05 V for the rest of the circuitry. The continuous current

TABLE II
PERFORMANCE SUMMARY AND COMPARISON WITH RECENT STATE-OF-THE-ART TRANSCEIVERS

	This work	ISSCC'15 [6]	JSSC'15 [8]	ISSCC'15 [5]	ISSCC'13 [3]	
CMOS node	28nm	40nm	55nm	40nm	90nm	
Data rate & modulation	1-Mbps GFSK	1-Mbps GFSK	1-Mbps GFSK	1-Mbps GFSK	1-Mbps GFSK	
RX noise figure (dB)	6.5	N/A	5.5	6.5	6	
RX sensitivity (dBm)	-95	-94	-94.5	-94.5	-98	
RX IIP3 (dBm)	-19	N/A	N/A	N/A	-19	
OSC FoM (dB)	188	183	179	N/A	183	
PLL in-band PN (dBc/Hz)	-92**	-90	N/A	N/A	-85	
	-101***					
Integrated PN (degree)	1.08**	1.5	N/A	N/A	2.3	
	0.87***					
TX max. Pout (dBm)	+3	-2	0	0	0	
Total PA efficiency	39%	25%	30%	<25%	N/A	
Direct antenna connection?	Yes	No	Yes	Yes	No	
Supply voltage (V)	0.5 [#] / 1	1	0.9-3.3	1.1	1.2	
Power consumption (mW)	TX @ 0dBm	3.7	4.2*	10.1	7.7	5.4
	RX	2.75	3.3	11.2	6.3	3.3
TX efficiency (P _{OUT} /P _{DC})	27%	15%	10%	13%	18%	
TRX Active area (mm ²)	1.9	1.3	5.76	1.1	3.68	

*Measured @-2dBm **FREF=5MHz ***FREF=40MHz [#]Low-voltage DCO & DPA

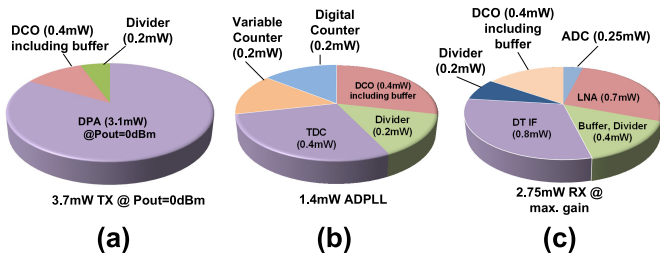


Fig. 21. Breakdown of measured power: (a) TX; (b) closed-loop ADPLL; (c) RX.

consumption of each RF/analog building block is individually measured from its supply pin. The TX consumes 3.7 mW at 0-dBm RF output. During actual TX and RX packets, most of the ADPLL is shut down immediately after settling. The DCO tuning word is then maintained on its update port, while the second port is used to perform an open-loop modulation (see Fig. 2). This reduces the LO power from 1.4 to 0.6 mW. The RX consumes 2.75 mW at maximum gain when sensitivity of -95 dBm is measured through PER curve of PER = 30.8% [8].

Table II summarizes the proposed TRX and compares it with recent state-of-the-art BLE designs. It is the first implemented in the 28-nm CMOS node. It reaches a similar RX performance (NF, linearity, and sensitivity) and a better TX performance (max P_{out}, PLL PN) but at a much lower power consumption, even better than [3] and [6], which use off-chip matching network and T/R switch. Compared with

the other two designs with fully integrated on-chip T/R switch [5], [8], the power efficiency is over 2× better for both the TX and RX.

VII. CONCLUSION

A single-chip ULP TRX for IoT applications, fully compliant with the BLE standard, is demonstrated in a digital 28-nm CMOS technology. The main objectives of this paper are: 1) full monolithic integration and 2) maximum power efficiency. Toward the first goal, active devices associated with a DCO and a PA are placed underneath their passive RF components to promote vertical integration of passive/active components as opposed to their almost exclusive lateral monolithic integration done conventionally. The TX and RX share a single pin for a direct connection to an antenna. Toward the second goal, we have implemented several power-saving techniques, taking advantage of the relaxed specifications defined in the standard. The TX directly modulates the DCO in an open-loop manner. The RX is a DT superheterodyne architecture performing amplification and filtering using CS complex-signaling BPFs.

REFERENCES

[1] Texas Instruments. (2015). *CC2640 SimpleLink Bluetooth Smart Wireless MCU*. [Online]. Available: <https://www.ti.com>
 [2] A. Wong *et al.*, "A 1V 5mA multimode IEEE 802.15.6/Bluetooth low-energy WBAN transceiver for biotelemetry applications," in *IEEE Int. Solid-State Circuits Conf. (ISSCC) Dig. Tech. Papers*, Feb. 2012, pp. 300-301.

- [3] Y.-H. Liu *et al.*, "A 1.9nJ/b 2.4GHz multistandard (Bluetooth low energy/ZigBee/IEEE802.15.6) transceiver for personal/body-area networks," in *IEEE Int. Solid-State Circuits Conf. (ISSCC) Dig. Tech. Papers*, Feb. 2013, pp. 446–447.
- [4] G. Devita *et al.*, "A 5mW multi-standard Bluetooth LE/IEEE 802.15.6 SoC for WBAN applications," in *Proc. Eur. Solid State Circuits Conf.*, Sep. 2014, pp. 283–286.
- [5] T. Sano *et al.*, "A 6.3mW BLE transceiver embedded RX image-rejection filter and TX harmonic-suppression filter reusing on-chip matching network," in *IEEE Int. Solid-State Circuits Conf. (ISSCC) Dig. Tech. Papers*, Feb. 2015, pp. 240–241.
- [6] Y.-H. Liu *et al.*, "A 3.7 mW-RX 4.4mW-TX fully integrated Bluetooth low-energy/IEEE802.15.4/proprietary SoC with an ADPLL-based fast frequency offset compensation in 40nm CMOS," in *IEEE Int. Solid-State Circuits Conf. (ISSCC) Dig. Tech. Papers*, Feb. 2015, pp. 1–3.
- [7] C. Bachmann *et al.*, "A 3.5mW 315/400MHz IEEE802.15.6/proprietary mode digitally-tunable radio SoC with integrated digital baseband and MAC processor in 40nm CMOS," in *Symp. VLSI circuits Dig. Tech. Papers*, Jun. 2015, pp. C94–C95.
- [8] J. Prummel, "A 10 mW Bluetooth low-energy transceiver with on-chip matching," *IEEE J. Solid-State Circuits*, vol. 50, no. 12, pp. 3077–3088, Dec. 2015.
- [9] F.-W. Kuo *et al.*, "A Bluetooth low-energy (BLE) transceiver with TX/RX switchable on-chip matching network, 2.75mW high-IF discrete-time receiver, and 3.6mW all-digital transmitter," in *Proc. IEEE Symp. VLSI Circuits (VLSI)*, Jun. 2016, pp. 1–2.
- [10] J. Masuch, and M. Delgado-Restituto, "A 1.1-mW-RX –81.4-dBm sensitivity CMOS transceiver for Bluetooth low energy," *IEEE Trans. Microw. Theory Techn.*, vol. 61, no. 4, pp. 1660–1673, Apr. 2013.
- [11] Bluetooth. (2014). *Bluetooth Specification Version 4.2*. [Online]. Available: <http://www.bluetooth.com>
- [12] J. Zhou, S. Jayapal, B. Busze, L. Huang, and J. Stuyt, "A 40 nm dual-width standard cell library for near/sub-threshold operation," *IEEE Trans. Circuits Syst. I, Reg. Papers*, vol. 59, no. 11, pp. 2569–2577, Nov. 2012.
- [13] R. B. Staszewski *et al.*, "All-digital TX frequency synthesizer and discrete-time receiver for Bluetooth radio in 130-nm CMOS," *IEEE J. Solid-State Circuits*, vol. 39, no. 12, pp. 2278–2291, Dec. 2004.
- [14] V. K. Chillara *et al.*, "An 860 μ W 2.1-to-2.7GHz all-digital PLL-based frequency modulator with a DTC-assisted snapshot TDC for WPAN (Bluetooth Smart and ZigBee) applications," in *IEEE Int. Solid-State Circuits Conf. (ISSCC) Dig. Tech. Papers*, Feb. 2014, pp. 172–173.
- [15] M. Tohidian, I. Madadi, and R. B. Staszewski, "A fully integrated highly reconfigurable discrete-time superheterodyne receiver," in *IEEE Int. Solid-State Circuits Conf. (ISSCC) Dig. Tech. Papers*, Feb. 2014, pp. 1–3.
- [16] I. Madadi, M. Tohidian, K. Cornelissens, P. Vandenameele, and R. B. Staszewski, "A high IIP2 SAW-less superheterodyne receiver with multistage harmonic rejection," *IEEE J. Solid-State Circuits*, vol. 51, no. 2, pp. 332–347, Feb. 2016.
- [17] F.-W. Kuo *et al.*, "A fully integrated 28nm Bluetooth low-energy transmitter with 36% system efficiency at 3dBm," in *Proc. ESSCIRC*, Sep. 2015, pp. 356–359.
- [18] M. Babaie *et al.*, "A fully integrated Bluetooth low-energy transmitter in 28 nm CMOS with 36% system efficiency at 3 dBm," *IEEE J. Solid-State Circuits*, vol. 51, no. 7, pp. 1547–1565, Jul. 2016.
- [19] M. Babaie, M. Shahmohammadi, and R. B. Staszewski, "A 0.5V 0.5mW switching current source oscillator," in *Proc. IEEE RFIC*, May 2015, pp. 183–186.
- [20] M. Shahmohammadi, M. Babaie, and R. B. Staszewski, "A 1/f noise upconversion reduction technique for voltage-biased RF CMOS oscillators," *IEEE J. Solid-State Circuits*, vol. 51, no. 11, pp. 2610–2624, Nov. 2016.
- [21] E. A. M. Klumperink, S. L. J. Gierkink, A. P. V. D. Wel, and B. Nauta, "Reducing MOSFET 1/f noise and power consumption by switched biasing," *IEEE J. Solid-State Circuits*, vol. 35, no. 7, pp. 994–1001, Jul. 2000.
- [22] S. Kee, I. Aoki, A. Hajimiri, and D. Rutledge, "The class-E/F family of ZVS switching amplifiers," *IEEE Trans. Microw. Theory Techn.*, vol. 51, no. 6, pp. 1677–1690, Jun. 2003.
- [23] F.-W. Kuo *et al.*, "A 12mW all-digital PLL based on class-F DCO for 4G phones in 28nm CMOS," in *IEEE VLSI Circ. Symp. Dig. Tech. Papers*, Jun. 2014, pp. 1–2.
- [24] B. Schulz, *Bluetooth Low Energy Measurements Using R&S CBTgo*, Rohde & Schwarz, Appl. Note 1MA200_3e, accessed on Jan. 27, 2017. [Online]. Available: <https://www.rohde-schwarz.com>
- [25] I. Aoki, S. D. Kee, D. B. Rutledge, and A. Hajimiri, "Distributed active transformer—A new power-combining and impedance-transformation technique," *IEEE Trans. Microw. Theory Techn.*, vol. 50, no. 1, pp. 316–331, Jan. 2002.
- [26] B. Soltanian, H. Ainspan, W. Rhee, D. Friedman, and P. R. Kinget, "An ultra-compact differentially tuned 6-GHz CMOS LC-VCO with dynamic common-mode feedback," *IEEE J. Solid-State Circuits*, vol. 42, no. 8, pp. 1635–1641, Aug. 2007.
- [27] C.-H. Lee *et al.*, "A 2.7 GHz to 7 GHz fractional-N LC-PLL utilizing multi-metal layer SoC technology in 28 nm CMOS," *IEEE J. Solid-State Circuits*, vol. 50, no. 4, pp. 856–865, May 1998.
- [28] A. Selvakumar, M. Zargham, and A. Liscidini, "Sub-mW current reuse receiver front-end for wireless sensor network applications," *IEEE J. Solid-State Circuits*, vol. 50, no. 12, pp. 2965–2974, Dec. 2015.
- [29] A. Mirzaei, H. Darabi, J. C. Leete, X. Chen, K. Juan, and A. Yazdi, "Analysis and optimization of current-driven passive mixers in narrow-band direct-conversion receivers," *IEEE J. Solid-State Circuits*, vol. 44, no. 10, pp. 2678–2688, Oct. 2009.
- [30] A. Mirzaei, H. Darabi, and D. Murphy, "A low-power process-scalable super-heterodyne receiver with integrated high-Q filters," *IEEE J. Solid-State Circuits*, vol. 46, no. 12, pp. 2920–2932, Dec. 2011.
- [31] A. Mirzaei, H. Darabi, J. C. Leete, and Y. Chang, "Analysis and optimization of direct-conversion receivers with 25% duty-cycle current-driven passive mixers," *IEEE Trans. Circuits Syst. I, Reg. Papers*, vol. 57, no. 9, pp. 2353–2366, Sep. 2010.
- [32] K. Muhammad, and R. B. Staszewski, "Direct RF sampling mixer with recursive filtering in charge domain," in *Proc. Int. Symp. Circuits Syst. (ISCAS)*, vol. 1, May 2004, pp. I-577–I-580.
- [33] S. Karvonen, T. A. D. Riley, S. Kurtti, and J. Kostamovaara, "A quadrature charge-domain sampler with embedded FIR and IIR filtering functions," *IEEE J. Solid-State Circuits*, vol. 41, no. 2, pp. 507–515, Feb. 2006.
- [34] R. Bagheri *et al.*, "An 800-MHz–6-GHz software-defined wireless receiver in 90-nm CMOS," *IEEE J. Solid-State Circuits*, vol. 41, no. 12, pp. 2860–2876, Dec. 2006.
- [35] B. Razavi, *RF Microelectronics*, 2nd ed. Englewood Cliffs, NJ, USA: Prentice-Hall, 2012.
- [36] M. Babaie and R. B. Staszewski, "A class-F CMOS oscillator," *IEEE J. Solid-State Circuits*, vol. 48, no. 12, pp. 3120–3133, Dec. 2013.
- [37] R. B. Staszewski and P. T. Balsara, *All-Digital Frequency Synthesizer in Deep-Submicron CMOS*. New York, NY, USA: Wiley, 2006.
- [38] S. B. Ferreira, F.-W. Kuo, M. Babaie, S. Bampi, and R. B. Staszewski, "System design of a 2.75 mW discrete-time superheterodyne receiver for Bluetooth low energy," *IEEE Trans. Microw. Theory Techn.*, vol. 65, 2017.



Feng-Wei Kuo was born in Kaohsiung, Taiwan, in 1976. He received the M.S. degree in electronics engineering from National Chiao Tung University, Hsinchu, Taiwan, in 2007. He is currently pursuing the Ph.D. degree with the Delft University of Technology, Delft, The Netherlands, as an external part-time student with the group of Prof. Staszewski.

In 2007, he joined the Design Technology Division, Taiwan Semiconductor Manufacturing Company (TSMC), Hsinchu, Taiwan, where he is currently involved in RF, analog and mixed-signal designs. He has authored more than five technical papers, and holds 20 granted patents. His current research interests include ultra-low-power transceiver and digital/analog phase-locked loops, delay-locked loops, and high-speed data-communication circuits design using advanced CMOS technology, as well as CMOS analog circuits.



Sandro Binsfeld Ferreira (S'11–M'16) received the B.S. degree in electronics engineering from the Technological Institute of Aeronautics, Sao Jose dos Campos, Brazil, in 1992, the M.S.E.E. degree from the Pontifical Catholic University of Rio Grande do Sul, Porto Alegre, Brazil, in 2005, and the Ph.D. degree in microelectronics from the Federal University of Rio Grande do Sul, Porto Alegre, in 2016.

From 2009 to 2014, he was an RF IC Design Instructor at the IC Brazil Program, in which a full curriculum in IC design was taught. In 2014, he was a Visiting Researcher at the Delft University of Technology, Delft, The Netherlands, under the direction of Prof. R. B. Staszewski. From 2014 to 2015, he was consulting for the RF Group of Taiwan Semiconductor Manufacturing Company, Hsinchu, Taiwan. His current research interests include analog and RF integrated circuits design, and the design and modeling of wireless communications systems.



Huan-Neng Ron Chen was born in Taichung, Taiwan, in 1982. He received the B.S. degree in electrical engineering from National Sun Yat-sen University, Kaohsiung, Taiwan, in 2004, and the M.S. degree in electronics engineering from National Chiao Tung University, Hsinchu, Taiwan, in 2006.

During his graduate study, he was involved in the development of RF transceiver. In 2007, he joined the Design and Technology Platform of Taiwan Semiconductor Manufacturing Company, Hsinchu, where he was involved in RF design and ADPLL for next-generation wireless/wireline applications.



Lan-Chou Cho was born in Taipei, Taiwan, in 1978. He received the B.S., M.S., and Ph.D. degrees in electrical engineering from National Taiwan University, Taipei, in 2001, 2003, and 2008, respectively.

He is currently with Taiwan Semiconductor Manufacturing Company, Hsinchu, Taiwan. His current research interests include phase-locked loops and high-speed CMOS data-communication circuits for multiple gigabit applications.



Chewn-Pu Jou received the B.S.E.E. and M.S.E.E. degrees from National Taiwan University, Taipei, Taiwan, in 1982 and 1984, respectively, and the Ph.D. degree from the State University of New York, Stony Brook, NY, USA, in 1991.

He was an RF designer for wireless LAN circuits and LTCC components with the Industrial Technology Research Institute, Hsinchu, Taiwan. In 1998, he initiated RFCMOS technology development at United Microelectronics Corporation. In 2001, he started Uwave tech. delivering RFCMOS wireless devices. Since 2006, he has been leading the Taiwan Semiconductor Manufacturing Company, Hsinchu, RF design team to help RF foundry business.

Dr. Jou was a recipient of the National Award of the 1997 Best MOEA Program.



Fu-Lung Hsueh (M'82–LM'17) received the B.S. and M.S. degrees in electrical engineering from National Chiao Tung University, Hsinchu, Taiwan, and the Ph.D. degree in electrical engineering from Lehigh University, Bethlehem, PA, USA.

He was with Sarnoff Corporation (formerly RCA Research Center), Princeton, NJ, USA, for 22 years. He is currently the Director of mixed-signal and RF solutions with the Design Technology Division, Taiwan Semiconductor Manufacturing Company (TSMC), Hsinchu, and is a fellow of the TSMC Academy. He has authored 75 papers and holds 89 issued patents. His current research interests include very large scale integration circuit designs in high-speed ADCs, phase-locked loops (PLLs), DACs, RF building blocks (LNA, VCO, and synthesizer), CMOS imaging sensors, CCD visible/UV imagers, high-speed interfaces, advanced PLL frequency synthesizers, high-density active-matrix electroluminescent display in silicon-on-insulator, infrared PtSi focal plane array imagers, single-event upset immune, and state-retention memories.

Dr. Hsueh was a TPC Member of A-SSCC from 2008 to 2011. He was an ISSCC TPC Member of Technology Direction during 2011–2015, the Session Chair and the Co-Chair from 2012 to 2014, and a Tutorial and Forum Coordinator from 2014 to 2015. He was a recipient of five Outstanding Technical Achievement Awards at Sarnoff in 1989, 1992, 1994, 1997, and 2002, three Chairman Innovation Awards at TSMC, and two best paper awards from SOI and SID conferences in 1994. He gave a Short Course at the 2012 Symposium on very large scale integration (VLSI) Circuits, Hawaii, and served as a Panelist of an evening Rump session at the 2013 Symposium on VLSI Circuit, Kyoto, Japan.



Iman Madadi (S'08–M'15) received the B.S.E.E. degree from the K. N. Toosi University of Technology, Tehran, Iran, in 2007, the M.S.E.E. degree from the University of Tehran, Tehran, in 2010, and the Ph.D. degree from the Delft University of Technology, Delft, The Netherlands, in 2015.

From 2013 to 2014, he was a Consultant at M4S/Hisilicon, Leuven, Belgium, where he designed a 28-nm 4G cellular superheterodyne receiver chip for cellular applications. Since 2015, he has been the Co-Founder and CTO of Qualinx B.V., Delft, developing low-power CMOS wireless chips. He holds seven patents and patent applications in the field of RF-CMOS design. His current research interests include analog and RF IC design for wireless communications.



Massoud Tohidian (S'08–M'15) received the B.Sc. (Hons.) degree in electrical engineering from the Ferdowsi University of Mashhad, Mashhad, Iran, in 2007, and the M.Sc. (Hons.) degree in electrical engineering from the University of Tehran, Tehran, Iran, in 2010, and the Ph.D. (*cum laude*) degree from the Delft University of Technology, Delft, The Netherlands.

He was a Researcher with the IMEP-LAHC Laboratory, Grenoble, France, from 2009 to 2010. He was a Consultant at M4S/Hisilicon, Leuven, Belgium, from 2013 to 2014, designing a 28-nm 4G cellular superheterodyne receiver chip for mobile phones. Since 2015, he has been the Co-Founder and CEO of Qualinx B.V., Delft, developing low-power CMOS radio chips. He holds eight patents and patent applications in the field of RF-CMOS design. His current research interests include RF transceivers, discrete-time/digital signal processing, phase-locked loop, and oscillators.



Mina Shahmohammadi (S'12–M'17) received the B.Sc. degree in communication systems from the Amirkabir University of Technology, Tehran, Iran, in 2005, the M.Sc. degree in electronics from the University of Tehran, Tehran, in 2007, and the Ph.D. degree from the Delft University of Technology, Delft, The Netherlands, in 2016.

From 2007 to 2011, she was an Analog Designer with Rezvan Engineering Company, Tehran, Iran. From 2011 to 2013, she was a Research Assistant with the Electronic Instrumentation Laboratory, Delft University of Technology, where she was involved in resistor-based temperature sensors. She continued her PhD work in 2013–2016 in Electronics Research Laboratory at TU-Delft on wide tuning range and low flicker noise RF-CMOS oscillators. Dr. Shahmohammadi is currently an Analog Designer with Catena, Delft. Her current research interests include analog and RF integrated circuits design.



Masoud Babaie (S'12–M'16) received the B.Sc. (with highest Hons.) degree in electrical engineering from the Amirkabir University of Technology, Tehran, Iran, in 2004, the M.Sc. degree in electrical engineering from the Sharif University of Technology, Tehran, in 2006, and the Ph.D. (*cum laude*) degree from the Delft University of Technology, Delft, The Netherlands, in 2016.

In 2006, he joined the Kavoshcom Research and Development Group, Tehran, where he was involved in designing tactical communication systems. From 2009 to 2011, he was a CTO of the company. From 2013 to 2015, he was consulting for the RF Group of Taiwan Semiconductor Manufacturing Company, Hsinchu, Taiwan, where he was involved in designing 28-nm all-digital phase-locked loop and Bluetooth low-energy transceiver chips. From 2014 to 2015, he was a Visiting Scholar Researcher with the Berkeley Wireless Research Center, Berkeley, CA, USA, with the Group of Prof. A. Niknejad. In 2016, he joined the Delft University of Technology as an Assistant Professor. His current research interests include analog and RF/millimeter-wave integrated circuits and systems for wireless communications.

Prof. Babaie was a recipient of the 2015–2016 IEEE Solid-State Circuits Society Pre-Doctoral Achievement Award. He serves as a reviewer for the IEEE JOURNAL OF SOLID-STATE CIRCUITS.



Robert Bogdan Staszewski (M'97–SM'05–F'09) was born in Bialystok, Poland. He received the B.Sc. (*summa cum laude*), M.Sc., and Ph.D. degrees in electrical engineering from the University of Texas at Dallas, Richardson, TX, USA, in 1991, 1992, and 2002, respectively.

From 1991 to 1995, he was with Alcatel Network Systems, Richardson, where he was involved in SONET cross-connect systems for fiber optics communications. In 1995, he joined Texas Instruments Incorporated, Dallas, TX, USA, where he was elected as a Distinguished Member of Technical Staff (limited to 2% of technical staff). From 1995 to 1999, he was involved in advanced CMOS read channel development for hard disk drives. In 1999, he co-started the Digital RF Processor (DRP) group within Texas Instruments with a mission to invent new digitally intensive approaches to traditional RF functions for integrated radios in deeply-scaled CMOS technology. From 2007 to 2009, he was a CTO of the DRP group. In 2009, he joined the Delft University of Technology, Delft, The Netherlands, where he currently holds a guest appointment of Full Professor (*Antoni van Leeuwenhoek Hoogleraar*). Since 2014, he has been a Full Professor with the University College Dublin, Dublin, Ireland. He has authored or co-authored four books, five book chapters, and 210 journal and conference publications, and holds 160 issued U.S. patents. His current research interests include nanoscale CMOS architectures and circuits for frequency synthesizers, transmitters, and receivers.

Prof. Staszewski has been a TPC Member of ISSCC, RFIC, ESSCIRC, ISCAS, and RFIT. He was a recipient of the 2012 IEEE Circuits and Systems Industrial Pioneer Award.